



RESEARCH ARTICLE

10.1029/2021GC010293

Biomagnetic Characterization of Air Pollution Particulates in Lahore, Pakistan

H. A. Sheikh¹ , B. A. Maher² , V. Karloukovski² , G. I. Lampronti¹ , and R. J. Harrison¹ ¹Department of Earth Sciences, Downing Site, Cambridge, UK, ²Centre for Environmental Magnetism and Palaeomagnetism, Lancaster Environment Centre, University of Lancaster, Lancaster, UK

Key Points:

- Microscopy and magnetic measurements of tree leaves indicate different sources of anthropogenic particulate air pollution
- First-order reversal curves can potentially be used as a proxy to identify particulate sources
- High concentrations of Fe-bearing ultrafine particles found in brake-pad and exhaust-pipe residue specimens

Supporting Information:

Supporting Information may be found in the online version of this article.

Correspondence to:

H. A. Sheikh,
has57@cam.ac.uk

Citation:

Sheikh, H. A., Maher, B. A., Karloukovski, V., Lampronti, G. I., & Harrison, R. J. (2022). Biomagnetic characterization of air pollution particulates in Lahore, Pakistan. *Geochemistry, Geophysics, Geosystems*, 23, e2021GC010293. <https://doi.org/10.1029/2021GC010293>

Received 9 DEC 2021

Accepted 9 JAN 2022

Author Contributions:

Conceptualization: H. A. Sheikh, R. J. Harrison**Data curation:** H. A. Sheikh**Formal analysis:** H. A. Sheikh, G. I. Lampronti, R. J. Harrison**Funding acquisition:** H. A. Sheikh, R. J. Harrison**Investigation:** H. A. Sheikh, R. J. Harrison**Methodology:** H. A. Sheikh, V. Karloukovski, G. I. Lampronti, R. J. Harrison**Project Administration:** H. A. Sheikh, R. J. Harrison**Resources:** B. A. Maher, V. Karloukovski, R. J. Harrison

© 2022. The Authors.

This is an open access article under the terms of the [Creative Commons Attribution License](https://creativecommons.org/licenses/by/4.0/), which permits use, distribution and reproduction in any medium, provided the original work is properly cited.

Abstract We report the characterization of anthropogenic magnetic particulate matter (MPM) collected on leaves from roadside *Callistemon* (bottlebrush) trees from Lahore, Pakistan, and on known sources of traffic-related particulates to assess the potential of first-order reversal curve (FORC) diagrams to discriminate between different sources of anthropogenic magnetic particles. Magnetic measurements on leaves indicate the presence of surface-oxidized magnetite spanning the superparamagnetic (<30 nm) to single domain (~30–70 nm) to vortex size range (~70–700 nm). Fe-bearing particles are present both as discrete particles on the surface of larger mineral dust or carbonaceous particles and embedded within them, such that their aerodynamic sizes may be decoupled from their magnetic grain sizes. FORC diagrams of brake-pad residue specimens show a distinct combination of narrow central ridge, extending from 0 to 200 mT, and a low-coercivity, vertically spread signal, attributed to vortex and multi-vortex behavior of metallic Fe. This is in agreement with scanning electron microscopy results that show the presence of metallic as well as oxidized Fe. Exhaust-pipe residue samples display a more conventional “magnetite-like” signal comprising a lower coercivity central ridge (0–80 mT) and a tri-lobate signal attributed to vortex state and/or magnetostatic interactions. The FORC signatures of leaf samples combine aspects of both exhaust residue and brake-pad endmembers, suggesting that FORC fingerprints have the potential to identify and quantify the relative contributions from exhaust and non-exhaust (brake-wear) emissions. Such measurements may provide a cost-effective way to monitor the changing contribution; of future particulate emissions as the vehicle fleet is electrified over the coming years.

1. Introduction

Epidemiological studies have associated particulate air pollution with reduced cognitive performance (Zhang et al., 2018), development of diseases in the pulmonary and cardiovascular systems (Devlin et al., 2014; Schwarze et al., 2006; Seaton et al., 1995), and dementia (H. Chen et al., 2017). The biological mechanisms behind higher risk of cardio-respiratory diseases in an air-polluted urban environment have been studied and associated with ultrafine particles (Leitte et al., 2012; Miller et al., 2017; Penttinen et al., 2001). The size, morphology, and chemical composition of particles are critical in gauging detrimental effects to human health. Conventional air pollution indices classify and monitor PM as a function of its aerodynamic diameter: Exposure to PM_{0.1} (≤0.1 μm), often referred to as ultrafine particles (UFPs), is of increasing focus and concern because of UFPs potential adverse health implications, as small particles can exert higher toxicity than larger particles (Ohlwein et al., 2019). UFPs can be drawn into the body via ingestion (Calderón-Garcidueñas et al., 2020), skin (Araviskaia et al., 2019), olfactory transport, and through the lungs, entering the alveoli and penetrating biological membranes, effectively translocating to almost all organs (Ohlwein et al., 2019; Schraufnagel, 2020). UFPs have been linked to cardiovascular, Alzheimer's disease (Smith et al., 1997), neurological, and chronic respiratory diseases (Calderón-Garcidueñas et al., 2016, 2019; Devlin et al., 2014; Maher, 2019; Maher et al., 2020; Rückerl et al., 2011). Particulates containing traces of heavy metals such as Zn, Cr, Mn, Fe, Cu, and Pb have adverse effects on human lung epithelial cells because of their high toxicity and their complex interactions with other metal contaminants (Yuan et al., 2019). Fe-bearing UFPs have been linked to respiratory diseases (Dusseldorp et al., 1995), mitochondrial dysfunction (Maher et al., 2020), and have also been found in human brain, where they may play a role, via the Fenton reaction, in the development of neurodegenerative diseases (Maher et al., 2016). The serious potential health impacts of Fe-bearing UFPs makes the use of magnetic measurements to characterize and monitor airborne particles a particularly powerful tool. Particle magnetic properties change fundamentally over the size range of nanometers to PM₁₀ and can be used to discriminate effectively between different magnetic phases. Therefore, both room temperature and low-temperature magnetic measurements have great potential for

Software: G. I. Lampronti, R. J. Harrison
Supervision: R. J. Harrison
Validation: H. A. Sheikh, B. A. Maher, R. J. Harrison
Visualization: H. A. Sheikh
Writing – original draft: H. A. Sheikh
Writing – review & editing: H. A. Sheikh, B. A. Maher, R. J. Harrison

discriminating between sources of PM. Moreover, by resolving different Fe minerals and their oxidation states (Fe^0 vs. Fe^{2+} vs. Fe^{3+}), the toxicity potential of Fe-bearing nanoparticles and their human health impacts can be determined (Gonet & Maher, 2019). Biomonitoring studies have correlated magnetic properties with PM_{10} and $\text{PM}_{2.5}$ concentrations (Hofman, Wuyts, Van Wittenberghe, Brackx, & Samson, 2014; Hofman, Wuyts, Van Wittenberghe, & Samson, 2014; Matzka & Maher, 1999; Muxworthy et al., 2003; Rea-Downing et al., 2020), transition and heavy metals such as Co, Sr, Zn, Ni, Pb, Ti (Hofman et al., 2020; Maher et al., 2008; Spassov et al., 2004) and polycyclic aromatic hydrocarbons (PAHs; Lehndorff & Schwark, 2004). A particle's size, surface area, and solubility are major determinants of its toxicity. Iron oxides and hydroxides are effective sorbents of heavy metals because of their large surface area (Cornell & Schwertmann, 2006). The toxicity potential of metals derived from traffic-related sources (exhaust and non-exhaust) has also been linked with the presence of endotoxins which can sit on particle surfaces and exacerbate the production of reactive oxygen species (ROS), with chronic health implications (Kelly & Fussell, 2012). Recent roadside (Gonet, Maher, & Kukutschová, 2021) and airborne brake wear (Gonet, Maher, Nyiró-Kósa, et al., 2021) characterization studies show that the contribution of Fe-rich particles from brake-wear emissions is very high compared to other particulate sources in urban macro-environments, and that more than 99% of brake wear particles are <200 nm. Therefore, a focus on Fe-bearing UFP is timely, and the use of magnetic properties as a tool for determining different sources of particulates is our primary goal.

Air quality in Lahore, Pakistan is one of the worst in the world, reaching unhealthy levels on most days according to the Air Quality Index (AQI) - which is based on the measurement of $\text{PM}_{2.5}$ and PM_{10} mass concentrations, as well as other major pollutants (ground level ozone, CO, NO_2 , and SO_2). However, these real-time but spatially restricted, mass-based measurements are unlikely to capture fully the adverse health risks posed specifically by Fe- and other co-associated metal-bearing UFPs. In this study, we aim to provide a morphological, chemical, and magnetic characterization of airborne particulate matter in Lahore and then apply magnetic approaches to identify and characterize Fe-particles and their sources. The lack of a standardized method to monitor these particles means that they can go undetected. We report the distinctive magnetic fingerprints of different PM sources (exhaust and non-exhaust emissions) and discuss the extent to which these can be detected and quantified using a biological proxy (bottlebrush leaves, in our study).

2. Materials and Methods

2.1. Sampling Campaign

The study site is located next to a heavily trafficked residential and commercial area of Canal Road, Lahore (Figure 1a). It consists of a divided highway—two sets of opposing lanes, separated by a canal -, lined by different species of trees. The chosen sampling site was a 22 m wide greenbelt adjacent to the west-bound carriageway, consisting of bottlebrush trees (*Callistemon*), an evergreen species, chosen because of its abundance in the vicinity (Figure 1a) and hair-like features on its leaf surface (Figure S16 in Supporting Information S1). The site was first visited on 10 February 2021 in order to mark the leaves which had started to grow approximately 10 days prior to the site visit. A mixture of both freshly grown leaves (estimated exposure time of 20–26 days) and leaves which had been exposed for approximately 1 year were collected. The height of tree crowns varied but as we are interested in exposure at inhalation height, we sampled at 1.5 m (which coincided with the base of the crown). Ten tree crowns were sampled by carefully picking leaves from the petiole during the period 17–26 February 2021; there was no rainfall recorded since the fresh leaves started growing. From each tree, we collected leaves facing away from and toward the road. From our trees of interest, 30 leaves were analyzed (lower than the expected 60 samples either because of absence of fresh leaves in some tree crowns or because some leaves were discarded by the Plant Health Protection Department). The leaves were kept in plastic bags and refrigerated for 2 weeks before magnetic and microscopic analysis. After initial magnetic analysis, the leaves were oven dried at 40°C for 2 days and powdered for low-temperature magnetic measurements and x-ray diffraction (XRD).

To characterize the particulates on leaves in terms of exhaust versus non-exhaust contribution, we collected residue samples from petrol exhaust pipes, diesel exhaust pipes, and brake pads of different vehicles in Lahore (Table S18 in Supporting Information S1). These were obtained by scraping an A4 sheet of paper on the inside of exhaust pipes and brake pads of cars, vans, and rickshaws. Microscopy and magnetic analysis were carried out on these residue samples on the paper to evaluate their contribution to the particles observed and measured for the leaves.

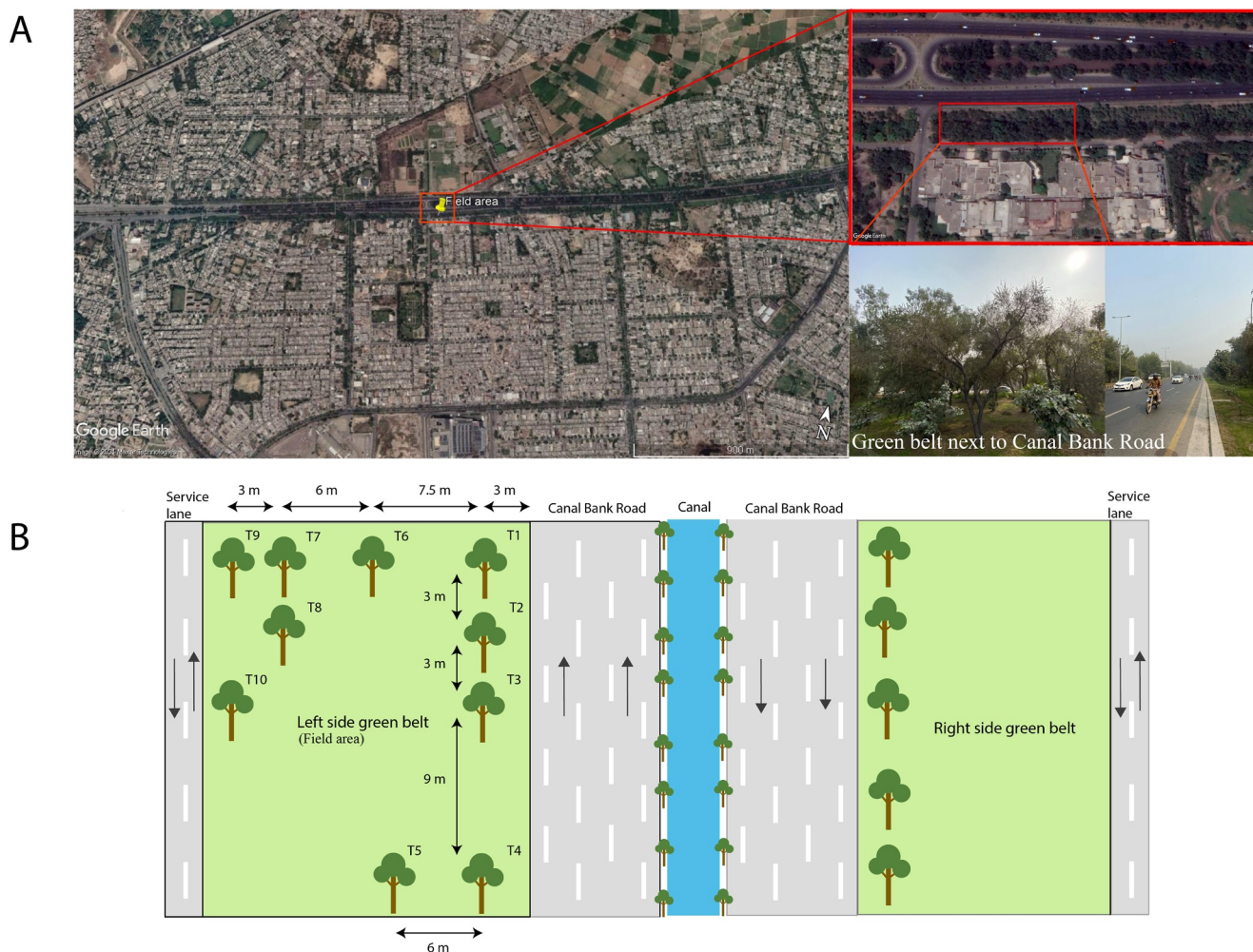


Figure 1. (a) Location of area of study and the nearby industrial estates and brick kilns. (b) Area of study showing the sampled trees and their distance from Canal bank road and the service lane.

2.2. Microscopy and Chemical Analysis

We performed backscattered electron (BSE) and secondary electron (SE) imaging and chemical characterization, using energy dispersive X-ray spectroscopy (EDX), of PM present in our leaves using a ThermoFisher Quanta-650F scanning electron microscope (SEM; nanometer resolution with magnification range 5–1,000,000X) equipped with two Bruker XFlash 6130 EDS detectors at the Department of Earth Sciences, University of Cambridge. Leaf specimens were carbon coated to prevent charging. Imaging was performed under high vacuum at both low accelerating voltages (2–5 kV) and high accelerating voltages (15 kV) using a spot size of 3.5–4.5. For microanalysis of ferro or ferrimagnetic minerals, we used 15 kV specifically to obtain the K-line excitation for Fe. This was performed to evaluate the morphology and chemistry of Fe-bearing minerals present and evaluate the association of magnetic carriers with other particulates.

2.3. X-Ray Diffraction

XRD measurements on powdered leaf specimens were performed in Bragg-Brentano geometry on a D8 Bruker diffractometer equipped with a Mo $K\alpha$ primary beam operating at 50 kV and 40 mA and a LYNXEYE XE-T position sensitive detector. Collection conditions: 2–30° 2θ range, 0.025° step size, 3 s/step, divergence slits 0.2.

2.4. Magnetic Analysis

The PM-laden leaves were analyzed for their bulk magnetic properties at the Centre for Environment Magnetism and Paleomagnetism (CEMP), Lancaster University. The surface area (m^2) of the leaves was determined, using a scanner, to normalize our results; the samples were wrapped in cling film and firmly pushed into 7 cm^3 polycarbonate pots for magnetic analysis. Leaf saturation isothermal remanent magnetization (SIRM) was normalized to surface area following Matzka and Maher (1999) and Kardel et al. (2011) because (a) deposition of PM on leaves depends mainly on the leaf surface characteristics and not its mass; (b) leaf surface area varies depending on light exposure in urban areas. A Molspin demagnetizer (with DC attachment) was used to impart an anhysteretic remanent magnetization (ARM) at 80 milliTesla (mT) alternating current (AC) field and 100 μT direct current (DC) bias field ($\text{ARM}_{80/100}$). Dividing ARM by the DC bias field yields the ARM susceptibility (χ_{ARM}). The samples were subsequently alternating field (AF) demagnetized at 10, 15, 20, 25, and 30 mT. A second set of measurements included acquisition of room temperature isothermal remanent magnetization (IRM) at 20, 100 mT using a Molspin pulse magnetizer; 300 mT and 1 T was acquired using a Newport electromagnet. The high-field remanent magnetization (HIRM) was used to calculate the relative contribution of hematite using the ratio $(\text{IRM}_{1000} - \text{IRM}_{300}) / \text{SIRM}_{1000}$, which assumes that all the IRM acquired between 300 and 1,000 mT is proportional to the amount of hematite present (Maher & Thompson, 1999). All remanence measurements were made at high speed of rotation on an AGICO JR-6A magnetometer (sensitivity $2.4 \times 10^{-6}\text{ Am}^{-1}$) with a metal shield option to create true zero field.

To help identify which magnetic phases are present on the leaf samples, we conducted low-temperature measurements on a Quantum Design Magnetic Property Measurement System (MPMS3) at the Maxwell Centre, University of Cambridge. Measurements were conducted on two leaf samples, two brake-pad samples and two exhaust-pipe samples according to the following sequence based on Lagroix and Guyodo (2017): (a) a room temperature SIRM (RT-SIRM) was imparted in a 2.5 T field and then measured on cooling from 300 to 10 K; (b) the RT-SIRM was then measured on warming back to 300 K; (c) the sample was zero-field cooled (ZFC) to 10 K and a low-temperature SIRM (LT-SIRM) imparted in a 2.5 T field; (d) the ZFC LT-SIRM was measured on warming to 300 K; (e) the sample was then field cooled (FC) in 2.5 T from 300 to 10 K and the resulting FC LT-SIRM was measured from 10 to 300 K. The instrument did not have a low-field cancellation option, and residual fields can range from 0.5 to 20 mT depending on the sequence used. Although the presence of a residual field complicates the interpretation of the curves (in particular, “ZFC” may not strictly be zero-field cooling and all “remanence” measurements may have an additional induced component of magnetization), the data are sufficient to achieve the primary goal of detecting the presence of a Verwey transition (Verwey, 1939) and the rapid loss of LT-SIRM on warming that may be associated with superparamagnetic (SP) particles.

Hysteresis parameters, DC demagnetization curves, and first-order reversal curves (FORCs; Pike et al., 1999; Roberts et al., 2000) were measured at room temperature using a Princeton Measurement Corporation MicroMag Accelerating Gradient Magnetometer (AGM) at the Nanopaleomagnetism Lab, University of Cambridge. Leaves, brake pad and vehicle exhaust pipe residue samples were cut into $4 \times 4\text{ mm}$ squares and mounted on the probe using grease. Due to the weak nature of the signals being measured, extra care was taken to account for any potential contamination of the AGM sample probe. A blank, greased probe measurement was taken before every hysteresis measurement to account for any remanence contribution from the probe; this blank measurement was averaged and subtracted from measured hysteresis loops. Multiple FORCs were acquired and averaged twice for each sample at 1 mT field step and an averaging time of 300 ms in discrete mode. FORC diagrams were processed using the VARIFORC algorithm (Egli, 2013) within the FORCinel software of R. J. Harrison and Feinberg (2008), with variable smoothing factors that are given in respective diagrams.

3. Results

3.1. Chemical, Crystallographic, and Morphological Classification of Leaf PM

The majority of the leaf-deposited PM we observed is “non-magnetic,” with variably geogenic, biogenic, or anthropogenic origins. We identified a total of nine particle types: mineral dust, carbonaceous particles, heavy metals, fly ash, soot, Ca-sulfate, secondary aerosol particles, biogenic particles (pollen), and Fe-bearing particles (Table S21 in Supporting Information S1; Figure 2). These particles were classified based on their elemental

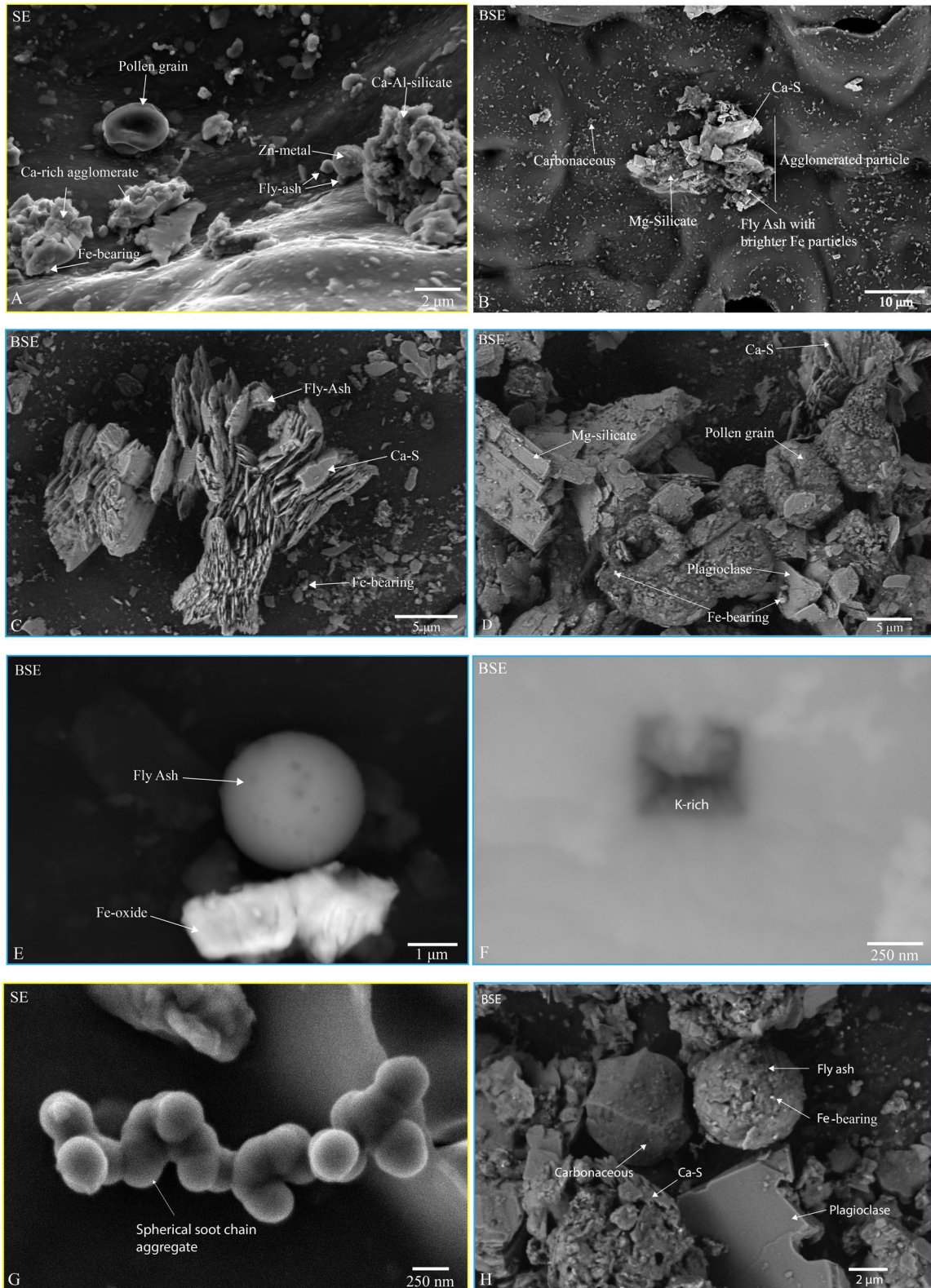


Figure 2.

composition using the EDX spectra and their morphology. To obtain a representative set of data, we looked at BSE images and EDX maps of leaf specimen T10-1Y-TSL (because it was exposed for an entire growing season) at four different horizontal field width (HFW) ranges—100, 30, 10, and 2 μm . For the size-focused classification of PM, 1,482 particles were analyzed and binned into different size ranges of >2.5 , 1.0–2.5, and <1.0 μm (Figure S1 in Supporting Information S1).

Mineral dust particles (e.g., Figures 2d and 2h) were the most abundant particles in the >2.5 μm leaf fraction. These particles were mostly irregular, sometimes agglomerated with other particles, and contained primarily Si, Al, Ca along with other associated elements, Fe, Mn, Mg, K, and F. Chemical phases recognized from EDX were Al-silicate (Figure 2a), Ca-Al silicate (Figure 2h), and XRD identified whewellite, anorthite (Ca-feldspar), and anhydrite (which could be both naturally occurring and/or anthropogenic; Figure S14 in Supporting Information S1).

Carbonaceous particles tended to display a range of morphologies, from spherical (Figure 2h) to irregular (Figure 2b). It was possible to distinguish anthropogenic carbonaceous particles from pollen grains based on their morphological features and sometimes from the presence of minor traces of K in the biomass burning-derived carbonaceous particles.

Heavy metals such as Zn (Figure S2 in Supporting Information S1), Ba (Figure S3 in Supporting Information S1) and metal oxides such as Ti-oxide (Figure S4 in Supporting Information S1) were observed in the SEM/EDX analysis. The particle sizes of metal-bearing particles ranged from 500 nm to 2.5 μm ; they occurred both as discrete particles and in association with Fe-oxides or silicates.

Fly ash particles had a characteristic smooth, spherical morphology, with size range usually between 1 and 2 μm . They contained primarily Si, Al, O, and were sometimes coated with aggregates of finer particles containing Fe, Mn, Mg, and Ca (Figure 2e).

Soot particles had a distinct chain-like morphology (Figure 2g) and were composed primarily of C spheres, typically 200 nm in diameter or smaller.

K-rich aerosol particles we observed were irregular-rectangular shaped, 0.5–2 μm in size, and were often coated with organic carbon (Figure 2f) or associated with soot (Figure S6 in Supporting Information S1).

Calcium sulfate (CaSO_4) particles (Figure 2c) were abundant and dominantly on the coarser end of the size spectrum (>2.5 μm) with a distinctive morphology of stacked, cleaved platelets.

Biogenic particles, such as pollen (Figures 2a and 2d), were classified separately from other carbonaceous particles. Pollen grains had a spherical-elliptical morphology and were dominantly coarser (>2.5 μm) with high C and O content. Whewellite (Figure S4 in Supporting Information S1) was also recognized as a biogenic particle, displaying euhedral particles in the size range 1–2 μm .

Fe-bearing particles on the leaf surfaces were present both as discrete particles and on the surface of (or embedded within) other metal- or non-metal-bearing particles (Figure 3). The diameter of Fe-bearing particles varied between <0.1 and 2.5 μm , with most particles ranging from <0.1 to 1.0 μm . In some cases, Fe-bearing particles were clustered together and sometimes associated with soot particles (Figure S5 in Supporting Information S1); BSE imaging showed that some ultrafine Fe-rich particles were embedded within silicates (Figure 3c).

Discrete Fe particles, usually in the range of 0.1–1.0 μm , were rounded-sub-spherical, while some of the spherical Fe-bearing particles had a dendritic-like texture and looked very similar to fly ash particles (Figure 3b). Fe particles were present both on the adaxial (upper) and abaxial (lower) side of the leaves, with a higher concentration on the adaxial side. EDX analysis showed all observed Fe-bearing particles were oxidized; in accord with our magnetic analysis (see Section 3.4) which confirmed the presence of surface-oxidized magnetite with a small contribution from a higher coercivity phase (potentially hematite).

Figure 2. Scanning electron microscope images of adaxial side of leaves. (a) Secondary electron (SE) image of fly ash particles clustered with Zn-rich spherical particle and Fe-bearing particle associated with Ca-sulfate agglomerate. (b) Backscattered electron (BSE) image of a calcium-sulfate agglomerate clustered together with fly ash having many Fe-bearing ultrafine particles on its surface. (c) Smooth platy-like gypsum particle. (d) Spherical pollen grains. (e) Smooth spherical fly ash particle. (f) K-rich rectangular particle. (g) Chain-like aggregate of soot particles. (h) Rectangular plagioclase, and a spherical carbonaceous particle. (Blue border: BSE, Yellow border: SE).

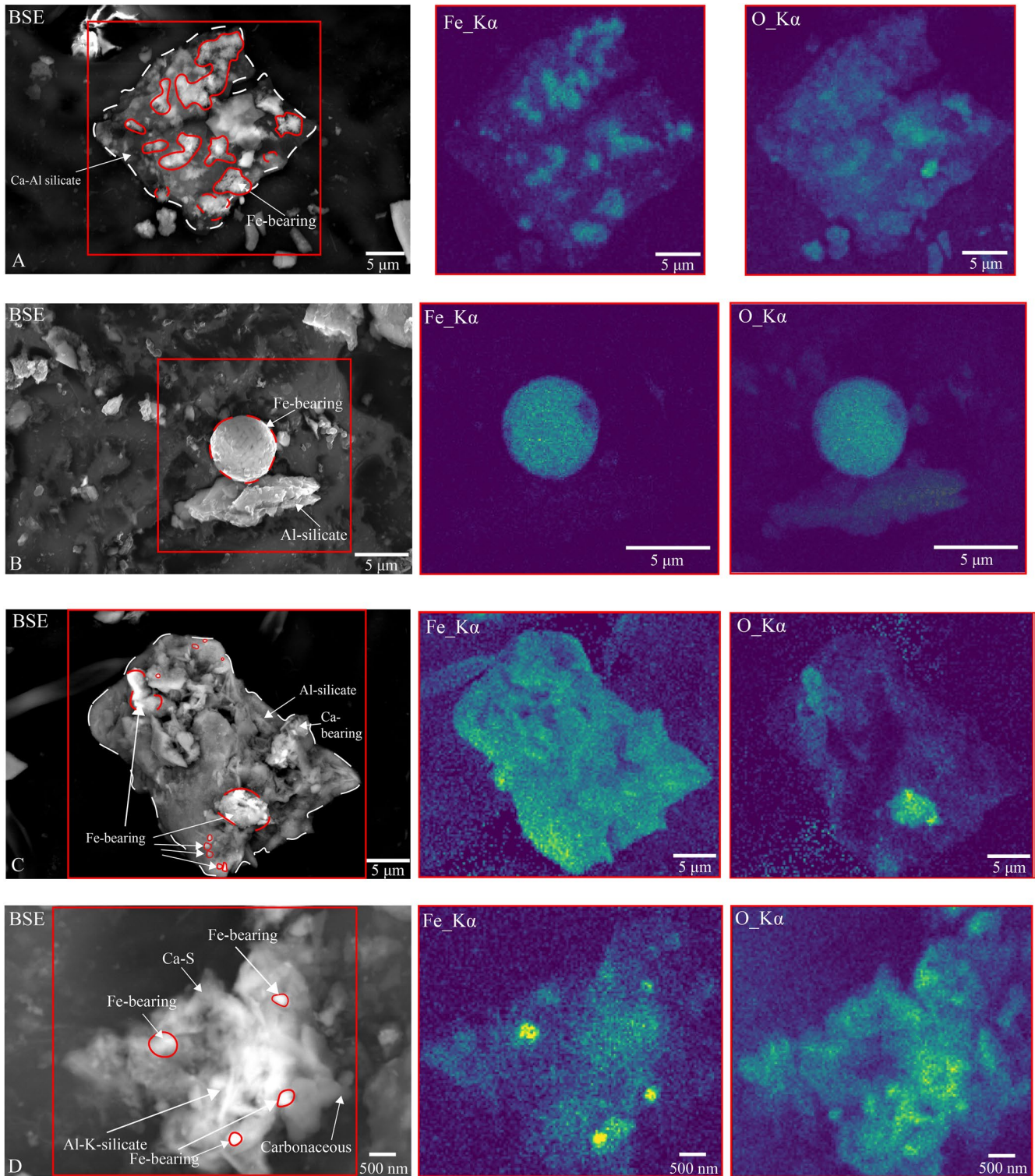


Figure 3. Scanning electron microscope images and EDX maps of Fe-bearing particles. (a) Cluster of Fe metal particles, ranging from 2.5 μm to less than 1 μm , embedded on surface of an Al-silicate; they exhibit a spiky ball morphology. (b) A spherical Fe-oxide particle (possibly from high temperature combustion) sitting on top of an Al-silicate. (c) Clusters of micron-sized Fe particles and a few discrete nanoparticles appear to be physically enclosed within a silicate particle. (d) Nano-sized Fe-bearing particles embedded within a silicate and carbonaceous agglomerate. (All images are BSE).

XRD patterns (Figure S14a–S14d in Supporting Information S1) for leaf sample T1_AW_1Y showed three major phases in the following abundance order: whewellite (calcium oxalate; Figure S5 in Supporting Information S1), anorthite (Ca-feldspar), and anhydrite. Calcium oxalate ($\text{CaC}_2\text{O}_4 \cdot (\text{H}_2\text{O})_x$) is a biomineral and can form in leaves as a way to regulate calcium levels in plant tissues and organs (Franceschi, 2001) by re-precipitating solubilized calcium (Glasauer et al., 2013). No Fe-oxide or Fe-metal peaks were observed.

3.2. Particles From Exhaust and Non-Exhaust Specimens

SEM/EDX analysis was conducted on residue particles collected from a Toyota Corolla XLI brake pad, Suzuki Alto brake pad, XLI petrol exhaust, and Mazda truck 3.5 L diesel exhaust pipe (Figure 4). The brake-pad specimen from a Toyota XLI showed abundant metallic Fe and Fe-bearing particles (Figure 4a). The particle sizes ranged from sub-micrometer to $>2 \mu\text{m}$. The EDX spectra of Fe-bearing particle (2) show an Fe-oxide within a silicate phase. Petrol exhaust-pipe residue samples (Figure 4b) show the presence of irregular Fe-bearing particles ranging in size from 0.5 to 3 μm ; EDX analysis of particle (3) shows a subhedral silicate particle enriched in Fe. EDX also identified the abundance of calcium-rich particles but also other anthropogenic metals such as Cr (Figure 4b). EDX for the Mazda truck 3.5 L diesel exhaust pipe particles showed the presence of finer Fe-bearing particles ($<2.5 \mu\text{m}$) within sulfur-rich carbonaceous particles ($>2.5 \mu\text{m}$; Figure 4c).

Heavy metals such as Mn, Al, and Cr of size ranges around 1–4 μm were also observed to be associated with Fe-bearing particles (Figures S11 and S12 in Supporting Information S1) in the XLI petrol exhaust specimen. The soot nanospheres observed on the leaves (Figure 2g) were also observed in the diesel exhaust pipe specimen (Figure S13 in Supporting Information S1) and were associated with Ca.

3.3. Leaf SIRM Variations

Both temporal and spatial variations in surface area specific SIRM were observed in tree crowns along the green belt (Figure 5). The higher magnetic signals were from samples collected closer to the main canal bank road or the service lane (Figure 5a) and exposed for the longest (~ 1 year). T1, facing toward the road, had a maximum SIRM value of 417.9×10^{-6} A. This was 7.5 times higher than a leaf exposed for 20 days and facing away from the road (56.2×10^{-6} A; Figure 5b). HIRM % of all our specimens was between 2.5% and 6%, suggesting some contribution from a high-coercivity magnetic component.

3.4. Low-Temperature Magnetic Properties

RT-SIRM and ZFC/FC LT-SIRM curves of powdered leaf specimens exposed for 1 year (T10_TSL_1Y) and 20 days (T10_TSL_20d) were measured and mass-normalized to see if there is any temporal variation in magnetic properties. Both specimens show a dampened Verwey transition at a temperature of around 115 K (Figure 6, Table 2). There is a weak but distinct partial recovery of remanence during warming back through the Verwey transition. The temperature-derivative of LT-SIRM curves of leaf specimens shows that remanence decreases swiftly from 10 to 60 K, more slowly from 60 to 100 K, followed by an acceleration of remanence loss at the Verwey transition. Both samples have FC $>$ ZFC remanence, with the difference between FC and ZFC persisting to a temperature of ~ 250 K.

RT-SIRM and ZFC/FC LT-SIRM curves of the XLI-brake-pad specimen are quite different to those of the leaf samples. Peak RT-SIRM occurs at 150 K rather than 200 K and shows a smaller remanence loss of 0.63% (at ~ 50 K) on cooling through the Verwey transition (Table 1). The temperature-derivative of LT-SIRM curves shows that remanence decreases swiftly from 10 to 60 K and more slowly from 60 to 300 K. FC versus ZFC difference is less pronounced than that for leaf specimens and there is no discernible difference for temperatures above ~ 100 K.

RT-SIRM and ZFC/FC LT-SIRM curves of the exhaust-pipe specimen are distinct from both leaf and brake-pad samples. A distinct kink in RT-SIRM at ~ 32 K is observed, which is reversible on warming. There is no distinct recovery of remanence associated with warming back through the Verwey transition, although the broad hump is largely reproduced. LT-SIRM curves show rapid acceleration of remanence loss from 30 to 60 K, with two

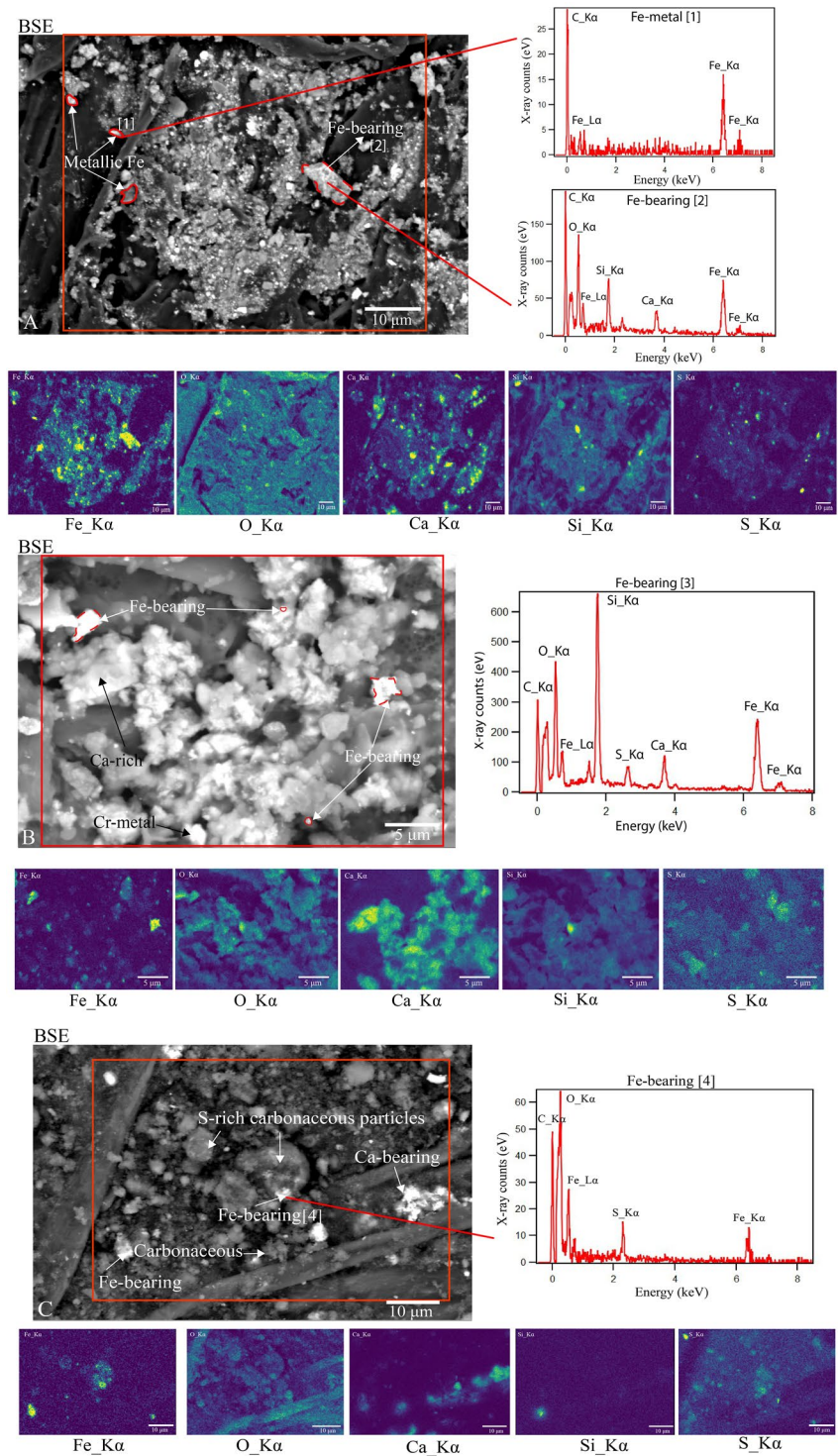


Figure 4. (a) Brake pad residue samples of XLI, showing nano-sized Fe-metal particles within silicate. EDX spectra for particles [1] shows the presence of metallic Fe and [2] oxidized Fe. (b) XLI petrol exhaust pipe residue showing irregular morphology of Fe particles; EDX spectra of particle [3] shows Fe-bearing particle embedded on top of a silicate (c) BSE image of Mazda truck 3.5 L diesel exhaust pipe residue showing nano-sized Fe-particles embedded on top of a silicate mineral and the corresponding EDX map [4] shows the presence of sulfur with Fe-bearing particles.

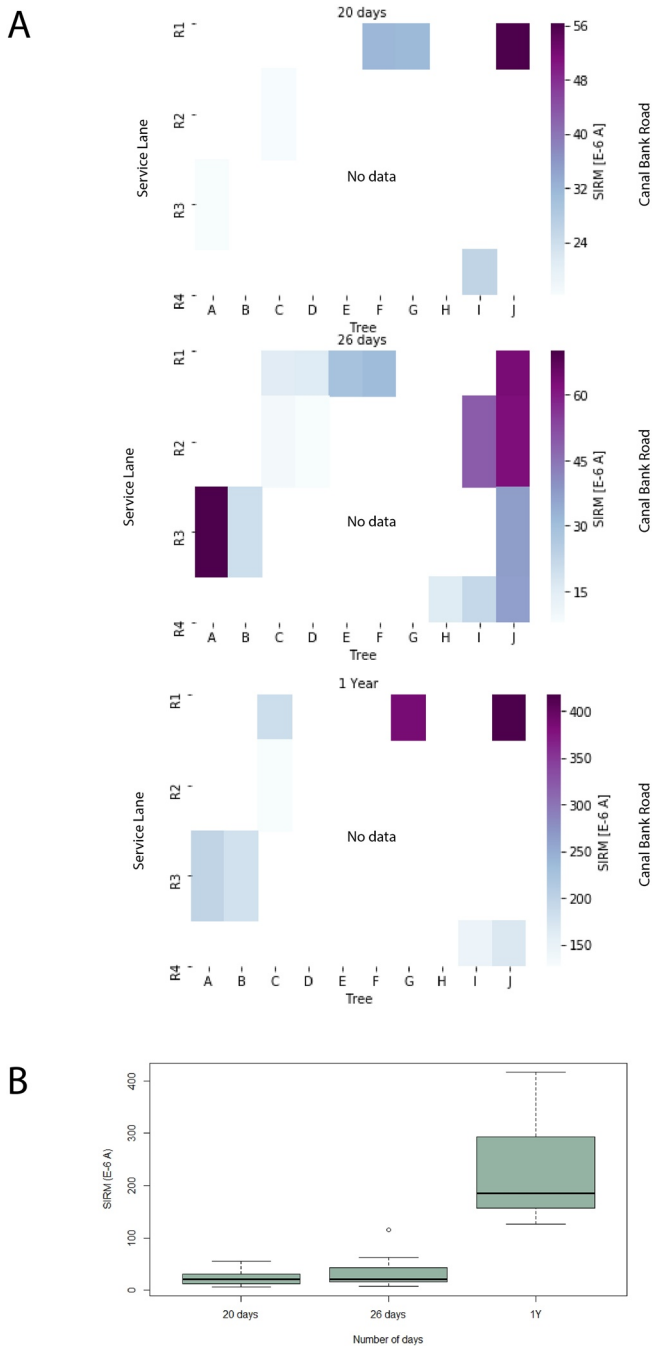


Figure 5. (a) Temporal and Spatial variation on measured leaf specimens (see Figure 1b for tree positions). Panel (b) shows the average saturation isothermal remanent magnetization values of leaf specimens over different timescales.

around a year, suggesting sources and resulting leaf magnetic mineralogy were similar (Figures S8a and S8b in Supporting Information S1).

Brake-pad specimens showed lower bulk coercivities (1.8–8.2 mT) compared to exhaust-derived specimens. Petrol exhaust pipe specimens had an average coercivity of 9.5 mT, and diesel exhaust pipe had average coercivity of 6.5 mT (Figure S8 in Supporting Information S1).

distinct peaks in the derivative of both FC and ZFC curves observed at 38 and 42 K. There is no visible acceleration of remanence loss at the Verwey transition. FC > ZFC remanence, with the difference persisting to at ~240 K.

A relative estimate of the superparamagnetic (SP) contribution in our specimens was calculated by comparing the ZFC LT-SIRM at 10 K to the RT-SIRM at 10 K. This measure provides an estimate of particles which are not capable of holding remanence when magnetized at room temperature (unblocked SP) but can hold a remanence when cooled to 10 K (blocked SP). Generally, the SP fraction in XLI brake pad and exhaust pipe specimens is higher than in the 1 year and 20-day leaf specimens (Table 2). For 1 year and 20 days leaf specimens, the RT-SIRM at 10 K represents 44% and 42% of LT-SIRM at 10 K, respectively. For the brake-pad and exhaust specimens, however, the RT-SIRM at 10 K represents just 7% and 13% of the LT-SIRM at 10 K, respectively, meaning that the remaining 93% and 87% of LT-SIRM remanence is carried by particles that were SP at 300 K and become blocked when cooled between 300 and 10 K.

3.5. Magnetic Granulometry

Assuming magnetite as the dominant ferrimagnetic component present, the room temperature $\chi_{ARM}/SIRM$ versus MDF_{ARM} Maher plot (Maher & Taylor, 1988; Maher et al., 2016; Figure 7a) shows that the specimens display a range of magnetite sizes, defining a loose trend bounded by single-domain (SD) grains (32–64 nm) at the fine end and multi-domain (MD) grains (7.5–17 μm) at the coarse end. Most of our leaf specimens lie within the field of interacting ultrafine magnetite grains. The old (1 year) versus the fresh (20 and 26 days) leaf particles group within the interacting magnetite grains region. Petrol exhaust pipe and brake pad samples also lie within the fine, interacting magnetite region whereas the diesel exhaust pipe falls in a coarser region. Figure 7b shows our specimen data plotted on the Lascu plot (Lascau et al., 2010). Our leaf specimens and diesel exhaust pipe specimen lie on the interacting single-domain (ISD) to multi-domain (MD) mixing line, in agreement with Figure 7a. The brake-pad abrasion residue specimens fall in the MD range. The petrol-exhaust pipe sample falls close to the “pseudo-single-domain” (PSD), also known as vortex (V) range.

3.6. Hysteresis and FORCs

Hysteresis properties of leaves and exhaust and non-exhaust sources were measured at room temperature and averaged over five times to reduce noise and drift. Parameters measured included saturation magnetization (M_s), saturation remanent magnetization (M_{rs}), and coercive force (B_c). DC-demagnetization curves were also measured at room temperature to obtain the remanent coercivity (B_{cr}). All leaf samples showed narrow hysteresis curves with coercivities (B_c) ranging from 2 to 15 mT (Figure S7 and Table S19 in Supporting Information S1). Specimens exposed for 20 and 26 days were weak and noisy but had similar hysteresis loop shape parameters to the samples exposed for

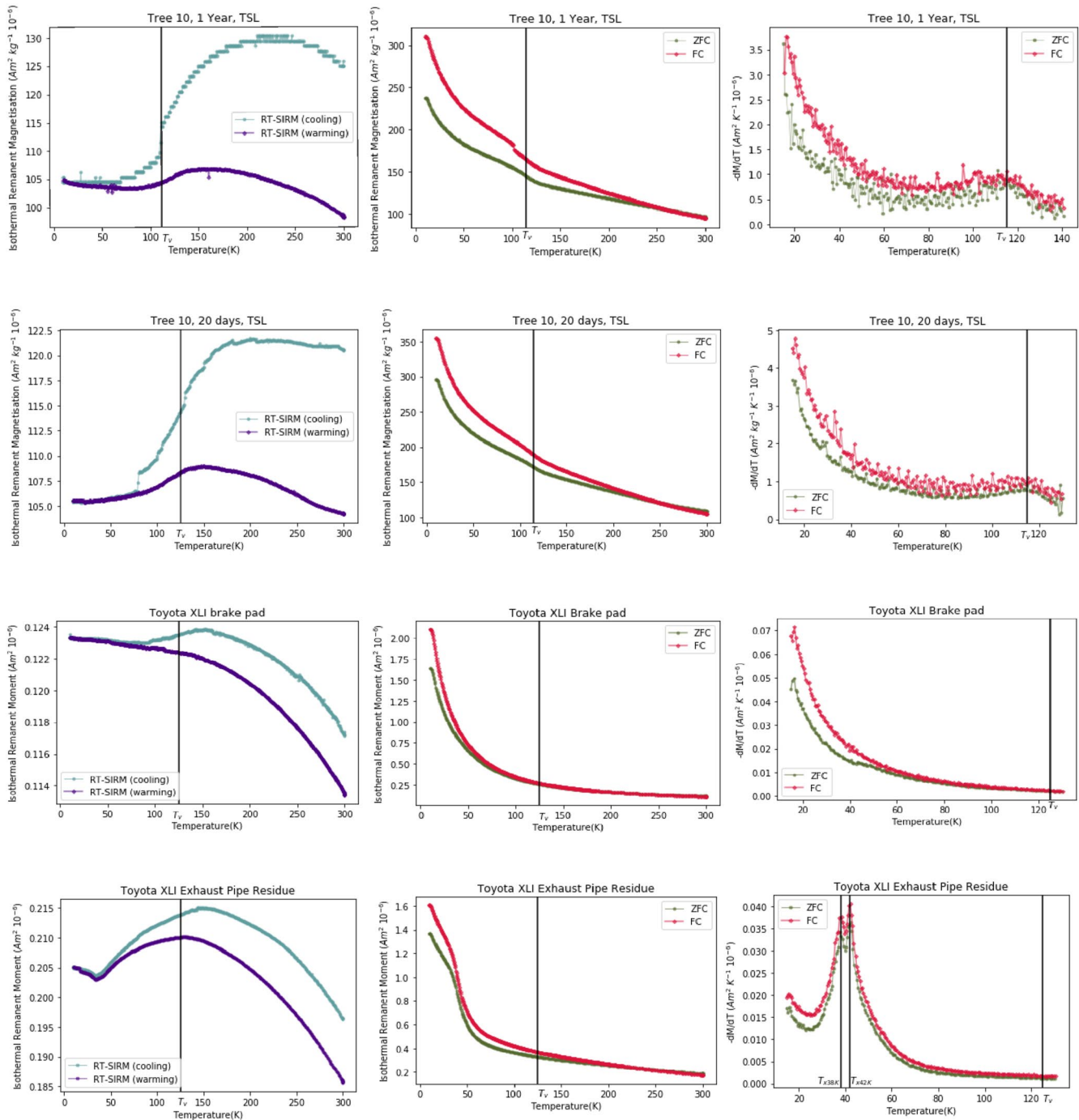


Figure 6. A 2.5 T DC field was applied to our samples to achieve room temperature saturation isothermal magnetic remanence (RT-SIRM). The samples were then cycled from 300 to 10 K and back to 300 K in zero-field, giving us two curves: RT-SIRM (cooling) and RT-SIRM (warming). ZFC-FC warming curves where IRM for FC was acquired at 2.5 T at 10 K. ZFC-FC curves show a peak at Verwey transition for leaf specimens at 115 K. RT SIRM cooling curve for XLI exhaust shows a peak at around 32 K, possibly hinting at pyrrhotite. Leaf specimens T10_1Y_TSL and T10_20d_TSL are mass normalized by dry weight of leaf powder measured using the gel cap; an accurate mass normalization was not possible for brake and exhaust-pipe specimens; therefore, absolute moment values are reported. Values for $-dM/dT$ versus temperature graph were taken from 12 K instead of 10 K because the temperature was not stabilized at low temperatures, hence contributing to slight curvature in $-dM/dT$ at 10–12 K.

We measured FORCs for all our specimens at the same parameters of 1 mT field step, 1 T saturation field, an averaging time of 300 ms: repeating the measurement twice to average FORCs. Leaf-specimen FORCs (Figure 8d) contain both low-coercivity (LC) and high-coercivity (HC) ridge signals, particles that are either strongly

Table 1
Room Temperature Measurements for Exhaust, Non-Exhaust, and Leaf Specimens

Specimen	T_v (K)	[RT-SIRM] _{10K} (Am ² 10 ⁻⁶)	[LT-SIRM] _{10K} (ZFC) (Am ² 10 ⁻⁶)	SP fraction (%) ^a	[RT-SIRM] _{MAX} (Am ² 10 ⁻⁶)	T at [RT-SIRM] _{MAX} (K)	[RT-SIRM-cooling] _{MIN} (Am ² 10 ⁻⁶)	Remanence loss (%) ^b
XLI-Brake pad	-	0.123	1.61	92.36	0.124	150	0.117	5.65
XLI- exhaust pipe	-	0.210	1.37	84.67	0.215	150	0.196	8.84

Note. The contribution of superparamagnetic grains is given by $[LT-SIRM]_{10K} - [RT-SIRM]_{10K} / [LT-SIRM]_{10K}$ and loss of remanence from peak SIRM at room temperature is given by $[RT-SIRM]_{MAX} - [RT-SIRM]_{MIN} / [RT-SIRM]_{MAX}$.

^a $[LT-SIRM]_{10K} - [RT-SIRM]_{10K} / [LT-SIRM]_{10K} \times 100$. ^b $[RT-SIRM]_{MAX} - [RT-SIRM]_{MIN} / [RT-SIRM]_{MAX} \times 100$.

interacting (Int) or in V states, and some contribution from SP grains. Less exposed leaves (in terms of both time and spatial positioning from traffic-related source) had lower magnetizable contribution and thus produced significantly noisier data, but near identical patterns of FORC distribution. The Alto brake-pad sample (Figure 8e) displays a high-coercivity ridge with SP contribution, and vertical spreading along the B_u axis, suggesting an MD signal. Exhaust-pipe signals were dominated primarily by a signal extending modestly along the horizontal B_c axis and some vertical spreading around the SP-SD ridge indicating the presence of Int and/or V states. Backfield IRM distributions ($-dM/d\log(B_c)$) were plotted against $\log(B_c)$; Figures 8a–8c). The backfield remanent coercivity distributions, extracted directly from the corresponding FORC data, showed that the brake pads are uniformly associated with the highest remanent coercivity component (blue), the exhaust pipe samples with the lowest remanent coercivity contribution (red), and that the leaves (black) have variable coercivity contributions that lie between these two extremes.

4. Discussion

4.1. Sources of Non-Magnetic Particles

Particle size distribution and morphological analysis using SEM/EDX (Figure 2) show a high contribution to the leaf-deposited particles from non-anthropogenic sources such as mineral dust, dominating the coarser end of the fine-particle spectrum ($<2.5 \mu\text{m}$). A previous source characterization study by Stone et al. (2010) in Lahore found that windblown mineral dust constituted $74 \pm 16\%$ of the coarser PM_{10-2.5} fraction. In arid areas, the most abundant natural dust mineralogy includes naturally occurring quartz, feldspar, clay minerals, and calcium carbonate (Claquin et al., 1999), all of which were observed in our SEM/EDX analysis (Figures 2a, 2b, 2d, 2e and 2h). Some proportion of the airborne calcium carbonate particles in Lahore is also likely to be anthropogenic and potentially related to coal power plant, construction industry, and cement production.

Anthropogenic particles such as carbonaceous particles, soot, heavy metals, secondary aerosol particles, and Fe-bearing particles dominate the leaf-deposited particles smaller than $<1 \mu\text{m}$. Sources of carbonaceous particles (Figure 2b) in urban areas have been linked to biomass burning, vehicular combustion, and industry (Saarikoski et al., 2008). In Lahore, carbonaceous and soot particles are likely to be related to fossil fuel combustion in vehicular engines, burning of crops, proximity to brick kilns, industry, and/or increased fuelwood burning during winter when demand for heating increases. Heavy metals in Lahore PM likely arise from industrial and vehicular emissions. A pollution characterization study in Islamabad, Pakistan found high enrichment factors (EF) for Sb, Zn, Cd, Pb, Cu, Co, Cr, and Mn and concluded that Co, Cr and Cu were related to metal industries while Pb, Cd, and Zn were from vehicular emissions (Shah et al., 2012). Zn, in particular, has been linked to exhaust, tire and road wear, brake wear emissions (R. M. Harrison et al., 2012), or smelting processes (Shaheen et al., 2005). The source of Zn in the leaf-deposited PM could be resuspended dust from the nearby traffic and/or from industries in Quaid-e-Azam Industrial or Sundar Industrial Estate.

The type of coal influences the chemical composition of fly ash, where lignite-sub bituminous coal has higher levels of Mg-oxides or Ca (e.g., Gaffney & Marley, 2009). Fly ash in Lahore was likely to be anthropogenic and could have originated from coal combustion in the nearby Master coal power plant, brick kilns or domestic use. A focused-ion-beam (FIB) study of fly ash by H. Chen et al. (2013) found Fe in the core of fly ash spherules, mainly in aluminosilicate phase. The same study found the Fe-bearing particles on the surface to be mainly Fe-oxides.

Table 2
Low-Temperature Measurements for Exhaust, Non-Exhaust, and Leaf Specimens

Specimen	T_v (K)	[RT-SIRM] _{10K} (Am ² kg ⁻¹ 10 ⁻⁶)	[LT-SIRM] _{10K} (ZFC) (Am ² kg ⁻¹ 10 ⁻⁶)	SP fraction (%) ^a	[RT-SIRM] _{MAX} (Am ² kg ⁻¹ 10 ⁻⁶)	T at [RT-SIRM] _{MAX} (K)	[RT-SIRM-cooling] _{MIN} (Am ² kg ⁻¹ 10 ⁻⁶)	Remanence loss (%) ^b
T10_TSL_1Y	115	104.0	240	56.60	129	200	104.0	19.37
T10_TSL_20d	115	105.5	295	64.40	122	200	105.5	13.52

Note. The contribution of superparamagnetic grains is given by $[LT-SIRM]_{10K} - [RT-SIRM]_{10K}/[LT-SIRM]_{10K}$ and loss of remanence from peak SIRM at room temperature is given by $[RT-SIRM]_{MAX} - [RT-SIRM]_{MIN}/[RT-SIRM]_{MAX}$.
^a $[LT-SIRM]_{10K} - [RT-SIRM]_{10K}/[LT-SIRM]_{10K} \times 100$. ^b $[RT-SIRM]_{MAX} - [RT-SIRM]_{MIN}/[RT-SIRM]_{MAX} \times 100$.

Calcium sulfate particles observed on the leaves are likely to have an anthropogenic origin from construction activities, cement industry, or nearby brick kilns. A previous study by Biswas et al. (2008) in Lahore argued that brick kilns are a major source of sulfate (SO₄²⁻) because of their use of low-grade (sulfur-rich) coal. A reaction of SO₄²⁻ ions with CaCO₃ is likely to be a secondary source of calcium sulfate.

K-rich particles have been identified as secondary organic aerosol (SOAs) particles (Figure 2f) and been related to biomass emissions (Silva et al., 1999) and used as a tracer for burning of crop residues (Niemi et al., 2006). Stubble burning after the harvest of the *Kharif* (summer) crop is prevalent in both India and Pakistan as farmers prepare to sow wheat for the winter season. Lahore experiences a “smog season” where haze and fog episodes concurrently occur in October to December. A source apportionment study in Lahore (Lodhi et al., 2009) claimed that during winter, crop burning, coal power plants, brick kilns, and traffic-related emissions increase the contribution from secondary aerosols in the lower atmosphere—accelerating the formation of smog. A study in Beijing on haze type by Li and Shao (2009) argued that particles such as soot, containing ultrafine metallic-Fe, are internally mixed in haze episodes and occur as inclusions within K or S-rich particles. The coating of organic carbon or soot with water-soluble particles such as nitrates of K-rich particles makes them hydrophilic (making them UFP hosts), eventually growing larger and more toxic as they are transported further distances (Li et al., 2010).

4.2. Biomagnetic Monitoring of Fe-Bearing UFPs

Magnetic analysis of leaf, brake pad, and exhaust pipe samples indicates the presence of a range of magnetic minerals, varying in their magnetizable content, grain size and morphologies. The results demonstrate that: (a) measured SIRM variations shows that leaf particulate accumulation increases over time (Day 0–26 exposure) within the tree canopies at 1.5 m, and hence can potentially be used for passive biomagnetic monitoring (Figure S15 in Supporting Information S1); (b) two of the potential sources of magnetic particles on roadside leaves have distinctive FORC signatures and coercivity distributions; and (c) these distinctive source signatures can be recognized in leaf samples, opening up the possibility of effective source attribution using FORC diagrams.

Leaf SIRM values increased with longer exposure time (Figure 5b). Lahore's average SIRM for year-long exposed leaves was 233×10^{-6} A, 20 days 24.2×10^{-6} A, and 40. 1×10^{-6} A for 26 days. These are very high compared with average SIRM values at inhalation heights reported in European cities (Table S20 in Supporting Information S1; Hofman, Wuyts, Van Wittenberghe, & Samson, 2014; Kardel et al., 2011; Mitchell & Maher, 2009; Muxworthy et al., 2002), 28.83×10^{-6} A (157 days) in Antwerp, Belgium (Hofman, Wuyts, Van Wittenberghe, & Samson, 2014), and 81×10^{-6} A in Lancaster, UK (exact exposure days not known but youngest leaves selected at 8 October 2007 after in-leaf season; Mitchell & Maher, 2009). The SIRM values for leaves from Lahore, Pakistan show a much higher magnetic loading in a lower number of days; however, differences in meteorological parameters, leaf species, deposition velocities and leaf accumulation capacity have not been calibrated against those of European biomagnetic studies, making quantitative comparisons of pollution levels difficult. A study by Maher et al. (2013) and Muhammad et al. (2019) on SIRM variability in leaf species claims that leaf trichomes (hair-like features) and surface area are important characteristics when it comes PM accumulation; where clusters of PM might occur in proximity to leaf hair. We see a temporal and spatial relationship (Figure 5) with SIRM, indicative of PM depositing on leaves. Roadside vegetation can inhibit airflow and influence nearby air quality

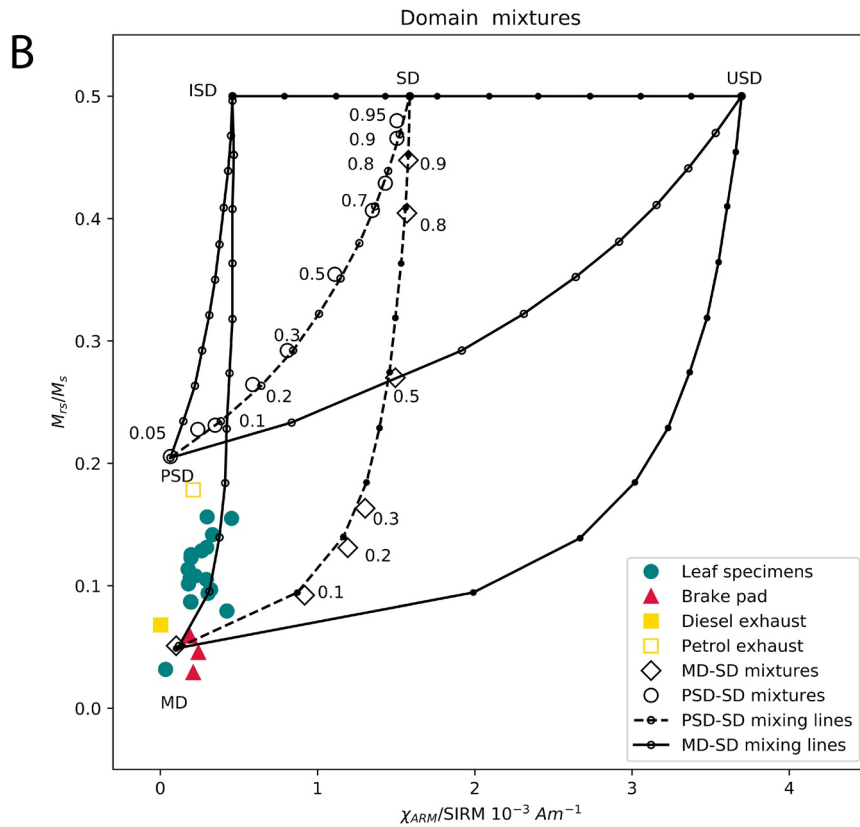
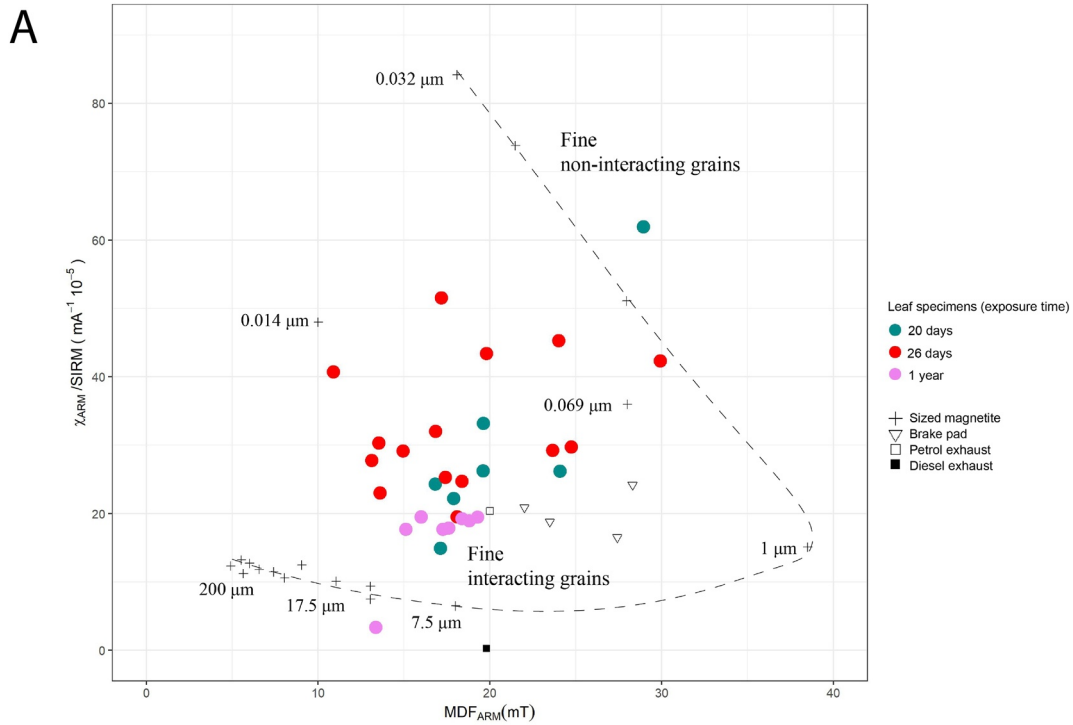


Figure 7.

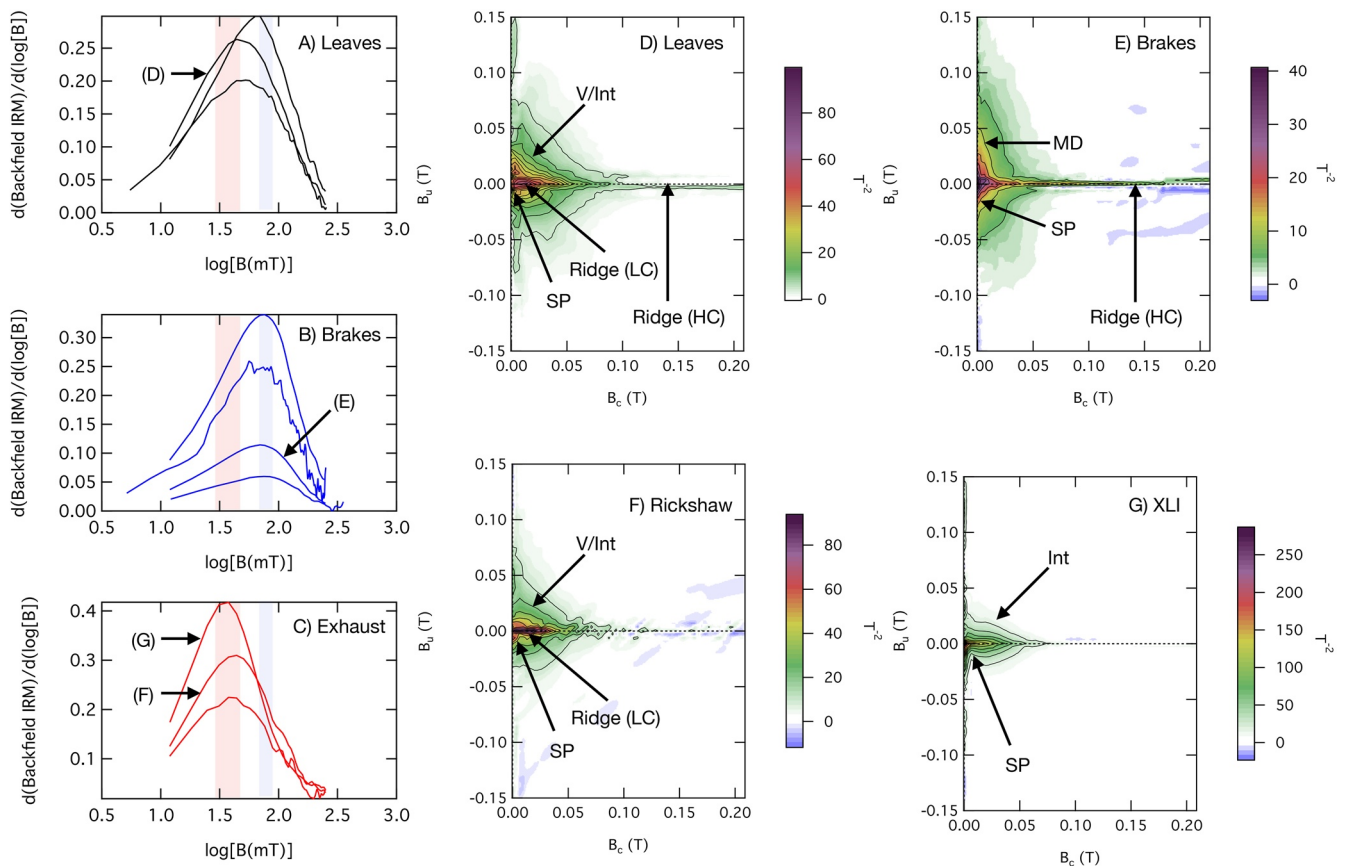


Figure 8. FORC diagrams and their coercivity distribution as a function of log(field). (a–c) Brake pads show the coercivities on the higher end of the distribution spectrum while exhaust pipe specimens are on the lower end. Leaf specimens lie in between both, suggesting it has contribution from both endmembers. (d) Average FORC of leaves showing presence of grains in vortex state, a low and high coercivity ridge (e) brake pad sample has a distinctive vertical distribution along the Bu axis., indicative of presence of MD grain sizes; FORC also shows a sharp SD tail extending to higher coercivity of 150–200 mT, suggestive of contribution from metallic Fe (see Figure 4a). (f) Rickshaw FORC shows a SD fingerprint with a PSD background. (G) XLI petrol exhaust shows interacting grains and an SP ridge. FORC = first-order reversal curve. FORC parameters used were field step (ΔH) = 1.5 mT, averaging time (t): 300 ms, $T = 300$. (d–g) FORC diagrams for leaves have been processed using VARIFORC smoothing (R. J. Harrison & Feinberg, 2008) using smoothing parameters $S_{c,0} = 10$, $S_{b,0} = 8$, $S_{c,1} = S_{b,1} = 12$, $\lambda: 0.3$; Brake dust residue: $S_{c,0} = 4$, $S_{b,0} = 4$, $S_{c,1} = S_{b,1} = 10$, $\lambda: 0.2$; Rickshaw exhaust residue: $S_{c,0} = 8$, $S_{b,0} = 8$, $S_{c,1} = S_{b,1} = 12$, $\lambda: 0.2$; XLI exhaust residue: $S_{c,0} = 6$, $S_{b,0} = 5$, $S_{c,1} = S_{b,1} = 10$, $\lambda: 0.3$.

by dispersing and/or depositing particulates on vegetation surfaces (Tong et al., 2016), and there is interest in the potential of green infrastructure to act as barriers and air filters when it comes to designing urban spaces. Leaf SIRM values in our study increased both with proximity to a vehicular source and longer exposure time (Figure 5a). For any given tree, the SIRM observed on the side facing toward the road is higher compared to that facing away from the road, indicating that deposition of PM on roadside leaves dominantly reflects traffic-related air pollution and that PM deposition occurs throughout the leaf canopy but is at a maximum closer to the PM source. Without further data, it is not possible to conclude from this study whether the reduced SIRM magnitude away from the road is due to the (a) “filtering effect” of trees (Jeanjean et al., 2017; Maher et al., 2013) or (b) the increased PM concentrations on the roadside of the vegetation barrier due to reduced air flow (Baldauf et al., 2008). In previous studies, up to ~50% reduction of PM₁₀ particles associated with roadside trees has been reported (Abhijith et al., 2017; Bealey et al., 2007; Maher et al., 2013; Wang et al., 2019). The proximal/distal

Figure 7. Panel (a) shows a comparison of leaf, brake pad and exhaust pipe specimens with sized magnetite grains (Dankers, 1978; Maher, 1988; Özdemir & Banerjee, 1982). This is represented by room temperature anhysteretic remanent magnetization (ARM) susceptibility (χ_{ARM}) normalized by saturation isothermal remanent magnetization (SIRM) versus the ARM mean destructive field (MDF_{ARM}) of each sample, which is defined when the magnetic fraction loses half of its remanent magnetization. It is indicative of the complicated relationship of mean grain size, where MDF_{ARM} increases with decrease in grain size. (b) Leaf, exhaust and non-exhaust specimens are plotted on the M_{rs}/M_s versus χ_{ARM}/M_{rs} for MD-SD (diamonds) and PSD-SD (circles) mixtures (Lascau et al., 2010). The numbers next to the symbols represent SD fraction in the total mixture.

SIRM difference is more pronounced for the 26-day data compared to the 1-year data, suggesting that magnetic loading may reach a steady-state value after prolonged exposure, irrespective of which side of the tree is sampled.

Leaf samples showed a dampened Verwey transition (Figure 6) at 115 K (lower temperature than the expected 120–125 K for stoichiometric magnetite) and rapid drop of remanence between 10 and 60 K, which is a signature of surface maghematization (Özdemir & Dunlop, 2010; Özdemir et al., 1993). No direct evidence of metallic Fe was found in the EDX data from leaves, so we assume that oxidized magnetite is the dominant magnetic mineral. It is possible that the primary magnetic source particles are metallic Fe and/or magnetite, both of which are oxidized when exposed to air over time. In particular, the 1-year exposed leaf specimen shows a more characteristic “hump” shape in cooling of RT-SIRM curve that is consistent with surface-oxidized magnetite (Özdemir & Dunlop, 2010); however, this is not as distinctive in the 20-day exposed leaf specimen. The drop at 70 K in 20-day leaf RT-SIRM (cooling) graph (Figure 6) is likely an artifact due to physical grain motion of the specimen during measurement. Magnetic granulometry, LT- versus RT-SIRM and FORC diagrams show a wide mixture of magnetic grain sizes in our samples—from SP (<30 nm) to SD (~30–70 nm) to V (~70–700 nm). A higher remanence for FC versus ZFC was observed for all our specimens and is consistent with (a) presence of magnetite and (b) grains dominated by SD rather than MD behavior. A previous study by Smirnov (2009) reported magnetite grain-size dependence as a function of the ratio of low-temperature SIRM (R_{LT} at 10 K) for FC and ZFC curves. The ratio for sized PSD particles is close to 1 and 1.27 for acicular magnetite. In our study, R_{LT} was around 1.3 for leaves, and 1.1 for brake-pad and petrol-exhaust pipe specimens—indicating the presence of both PSD and SD magnetite. There is little evidence of a strong MD (>1 μm) signal in the FORC diagrams, despite direct observation of magnetite spherules >1 μm in the SEM (e.g., Figure 3b). This apparent contradiction may be explained by the dendritic form of these magnetite grains, which is likely to reduce the effective grain size to <1 μm and introduce a strongly interacting component. Our leaf specimens broadly lie on the ISD-MD mixing line of Figure 7b, rather than the expected ISD-PSD mixing line. Note, however, these methods likely overestimate the MD component due to the presence of a significant SP fraction (identified by the comparison of LT- vs. RT-SIRM), which will shift the observed M_{rs}/M_s from PSD reference values toward MD reference values. The dominant grain size of magnetic particles from specimens in this study is spread over both interacting and non-interacting fine grain sizes, a wider range compared to that previously reported in studies in Lancaster (0.1–1.0 μm ; Mitchell & Maher, 2009) and Munich (0.1–0.7 μm ; Muxworthy et al., 2002).

Our leaf and exhaust residue specimens lie within the PSD range on the Day plot (Table S18 in Supporting Information S1, Day et al., 1977), while the brake pad residue specimens lie between theoretical magnetite SP-SD and MD mixing lines (Dunlop, 2002). Previous biomagnetic studies on leaves (Sagnotti et al., 2009) and lichens and leaf specimens (Winkler et al., 2020, 2021) show that their specimens lie closer to brake dust specimens than exhaust specimens. The higher proportion of exhaust emissions shown in our leaf specimen data might be due to (a) the sampling site being located next to a road section where cars flow freely with minimal braking; (b) oxidation of metallic Fe derived from brake pad dust over time in our leaf specimens; (c) a different profile of vehicle use in Lahore, which has a higher proportion of small, light vehicles such as rickshaws, which may produce higher exhaust emissions relative to brake dust emissions. Gonet, Maher, and Kukutschová (2021) also argue that particulate characteristics may change street to street and brake-derived PM is likely to have low contributions at a road where there is free-flowing traffic such as a highway.

4.3. Exhaust and Non-Exhaust Sources

Magnetic granulometry results place our brake-pad specimens near the MD region (Figure 7b). Although this matches a MD component visible in the FORC diagrams, and the low bulk coercivity of the brake-pad samples, it fails to reflect the presence of much finer grain size fractions associated with the presence of a high-coercivity ridge, and the fact that brake-pad residue specimens display the highest coercivity peak in the backfield remanent coercivity distribution plots (Figure 8b). This failure is partly due to the well-documented problems of using bulk average parameters such as M_{rs}/M_s to characterize mixtures of different domain states (Roberts et al., 2018), and partly due to the fact that the mixing lines on the granulometric plots are designed for magnetite, whereas FORC diagrams and SEM observations indicate the presence of metallic Fe in the brake pad particles. The high-coercivity ridge that is common to all brake-pad samples can be interpreted in a number of ways. Such ridges are normally associated with non-interacting, uniaxial SD behavior (Egli et al., 2010). However, these SD signals should also be accompanied by a distinctive $-ve/+ve$ background signal (Newell, 2005), which is absent from the

observed brake-pad FORC diagrams. Furthermore, if the high-coercivity ridge signal was due to SD magnetite, and the low-coercivity, vertically spread signal due to MD magnetite, one would expect intermediate grain sizes spanning the V state to create a characteristic tri-lobate signal (Lascu et al., 2018). Such a signal is present in the exhaust samples (e.g., Figure 8f) but absent from the brake-pad FORCs. The result is a rather unusual bimodal combination of high-coercivity ridge and a low-coercivity, vertically spread signal, which is more consistent with nanoscale particles of metallic Fe (Lappe et al., 2011, 2013). Micromagnetic simulations by Einsle et al. (2018) demonstrate that both the high-coercivity component of the ridge and the vertically spread signals can be explained by the nucleation and annihilation of vortex states in metallic Fe particles with sizes from 32 nm up to several hundred nanometers. Hysteresis measurements show that the brake-pad specimens have the lowest bulk coercivity values (Figures S8 and S9 in Supporting Information S1), but the highest distribution of remanence coercivities (Figure 8b). This observation is explained by the simulations of Einsle et al. (2016), which demonstrate that bulk coercivity values for V-state metallic Fe are extremely low, whereas switching fields associated with V-state nucleation and annihilation are very high. A failure to appreciate this difference may lead to erroneously attributing low-coercivity components in IRM unmixing plots to brake-pad related PM source contributions. The low-coercivity component of the ridge may be generated by SD particles (23–200 nm; Lappe et al., 2011; Muxworthy & Williams, 2015), with the region near the origin associated with those particles approaching the SP/SD limit (<23 nm; Nagy et al., 2019). Given the >90% loss of LT-SIRM on heating from 10 to 300 K (Figure 6c), a high proportion of particles are expected to be <23 nm (SP) in size and are likely poorly characterized by our SEM imaging. The high SP contribution from exhaust and non-exhaust residue specimens and leaves (Tables 1 and 2) is consistent with the 80% SP fraction estimate by low-temperature measurements conducted by Sagnotti et al. (2006) on motorway dust samples from Switzerland (Spassov et al., 2004). Our observations support the evidence that brake wear is a major source of Fe-bearing UFPs, which may pose serious risk to human health (Gonet, Maher, Nyiró-Kósa, et al., 2021).

For the Toyota XLI exhaust pipe specimen, the steep decrease in RT-SIRM value at 32 K (Figure 6d) may be related to the presence of pyrrhotite ($\text{Fe}_{(1-x)}\text{S}$) (Dekkers et al., 1989), which can be related to the presence of high-sulfur content in fuel oil. However, ZFC-FC curves do not show such a feature but instead two peaks at 38 and 42 K, hinting at the presence of some other unidentified magnetic mineral(s).

Common features include a low-coercivity ridge extending from 0 mT (SP) to ~80 mT (SD), and a tri-lobate feature (V and/or magnetic interactions). The FORC diagram of the rickshaw exhaust (Figure 8f) most closely resembles those of some leaf samples (Figure 8d), with near identical peak positions in the backfield remanent coercivity distribution (Figures 8a and 8c). Toyota XLI exhaust sample shows a more distinct FORC diagram with a clear SP signature (Lanci & Kent, 2018) and an interacting SD signal (R. J. Harrison & Lascu, 2014). The lack of a V-state tri-lobate feature indicates a finer grain size distribution in comparison to our typical diesel FORCs (Figure S10 in Supporting Information S1). The distinctive nature of the FORC diagrams raises the possibility that FORC diagrams may be capable of not only discriminating between exhaust and non-exhaust emissions, but between different types of exhaust emissions themselves.

The relative uniformity of the backfield remanent coercivity distributions observed in different brake-pad and exhaust-pipe samples contrasts with the more variable, intermediate distributions observed in the different leaf samples. On average, the leaf FORCs more closely resemble those of the exhaust-pipe than the brake-pad samples, although some leaves were observed with a more prominent high coercivity (HC) ridge and backfield remanent coercivity distributions that approach the high values of the brake-pad samples. However, FORCs of PM_{10} filters in Rome and Milan, Italy (Winkler et al., 2020), and lichens in Rome, Italy (Winkler et al., 2021) suggested dominant contribution from non-exhaust (brake wear) sources. This observation is consistent with the Day plot data discussed above and the explanations are the same. Together, these observations suggest that the leaf samples represent variable contributions from (at least) these two sources, and that (in principle) the contributions from each could be quantified using approaches such as FORC-PCA (R. J. Harrison et al., 2018; Lascu et al., 2015). Two complications that would need to be addressed first, however, are (a) the relatively high noise levels of the FORC data for such weak samples, and (b) the possibility that metallic-Fe particles generated by brake wear become oxidized over time, so that their contribution to the FORC diagram of a leaf sample is modified relative to that in the pure brake-pad end member. These issues will be tackled in a future study.

4.4. Outlook

Fe-bearing nanoparticles are highly toxic; for example, magnetite's bioreactive Fe^{2+} may disrupt the redox balance and damage cells (Maher et al., 2020); the presence of Fe-catalyzed free radicals have been linked to increasing oxidative damage in development of Alzheimer's disease. A recent study on brake abrasion dust (BAD) shows that particles from brake pads with metallic content (abundant in Fe) provoke an inflammatory response in human airways (Selley et al., 2020). Observations from the SEM also show the association of nano-sized Fe-particles with transition metals, and toxicological studies have suggested that metal-rich UFPs have been able to access all major organs (Nel et al., 2006), and cause acute pulmonary health implications (Dreher et al., 1997).

The nature of nano-sized particles is such that humans are susceptible to their exposure and the higher toxicity of metals, such as Fe. For this reason, it is essential that their contribution in ambient PM is quantified across the urban environment where most people are most exposed to them. Magnetic measurements are an effective way to detect the presence of and differentiate between these particles. The variation in magnetic signatures of exhaust and non-exhaust sources as observed in FORCs, low-temperature magnetic measurements, and microscopy shows the potential importance of the technique to quantify the contributions from these sources. As the world tackles climate change and air pollution, countries are pushing for a transition to electric vehicles (EV)—although a move to EV will bring exhaust emissions to near-zero, the relative contribution from non-exhaust (brake, tyre, and road wear) sources is likely to increase. The methods outlined here may provide a cost-effective way to monitor the changing contributions to roadside particulate pollution levels over the coming decades.

5. Conclusions

Lahore is the second most polluted city in the world in terms of $\text{PM}_{2.5}$ and PM_{10} , but the largest weight fraction of such particles constitutes of mineral dust and carbonaceous particles. Recent epidemiological studies have revealed acute health concerns arising from exposure to UFP and toxic heavy metals such as Fe, highlighting the need to quantify and characterize this particle size fraction. Using magnetic protocols and high-resolution microscopy, we have been able to characterize the composition, size, and origin of PM deposited on roadside leaves, and to distinguish between two major traffic-related sources of PM in Lahore. SEM and EDX data show that Fe-bearing particles are mainly oxidized magnetite and Fe-metal, contributing to the magnetic signal in our roadside leaves. Our FORC results show distinctive fingerprints for exhaust and brake wear residue particulates, which appear to be the two major contributions to the magnetic signal on the leaves. We confirm the presence of a significant nano-sized ferrimagnetic fraction both on the roadside leaves and in the exhaust and brake wear samples by conducting low-temperature magnetic measurements. The SP contribution of these nanoparticles is not observable in SEM or room temperature magnetic methods, but these nano-sized particles may have serious health implications. PM levels reported by traditional, mass-based metric systems are quick and real-time, but they fail to take into account the complex compositions, morphologies, and interactions of particulates, and especially of the nanoparticles, with serious potential implications in adverse health outcomes including cardiovascular, respiratory, and neurodegenerative diseases. Our magnetic and microscopy data emphasize the potential for increased magnetic quantification and differentiation of PM sources at a range of spatial and temporal scales.

Data Availability Statement

The magnetic raw data measured at room and low temperature is available at Zenodo via (<https://doi.org/10.5281/zenodo.5733952>) with open access.

References

- Abhijith, K., Kumar, P., Gallagher, J., McNabola, A., Baldauf, R., Pilla, F., et al. (2017). Air pollution abatement performances of green infrastructure in open road and built-up street canyon environments – A review. *Atmospheric Environment*, 162, 71–86. <https://doi.org/10.1016/j.atmosenv.2017.05.014>
- Araviiskaia, E., Berardesca, E., Bieber, T., Gontijo, G., Sanchez Viera, M., Marrot, L., et al. (2019). The impact of airborne pollution on skin. *Journal of the European Academy of Dermatology and Venereology*, 33(8), 1496–1505. <https://doi.org/10.1111/jdv.15583>
- Baldauf, R., Thoma, E., Khlystov, A., Isakov, V., Bowker, G., Long, T., & Snow, R. (2008). Impacts of noise barriers on near-road air quality. *Atmospheric Environment*, 42(32), 7502–7507. <https://doi.org/10.1016/j.atmosenv.2008.05.011>

Acknowledgments

H. A. Sheikh would like to thank Muhammad Rafiq, local gardener in Lahore who knew everything about the trees on Canal Bank Road; Dr. Iris Buisman for help with coating samples and SEM sessions; Dr Cheng Liu at Maxwell Centre for training me on the MPMS. H. A. Sheikh would also like to thank Plant Health Protection Authority in Lahore, Pakistan for providing a phytosanitary certificate for the leaf specimens and the Cambridge Trust for PhD funding.

- Bealey, W., McDonald, A., Nemitz, E., Donovan, R., Dragosits, U., Duffy, T., & Fowler, D. (2007). Estimating the reduction of urban PM₁₀ concentrations by trees within an environmental information system for planners. *Journal of Environmental Management*, 85(1), 44–58. <https://doi.org/10.1016/j.jenvman.2006.07.007>
- Biswas, K., Ghauri, B., & Husain, L. (2008). Gaseous and aerosol pollutants during fog and clear episodes in South Asian urban atmosphere. *Atmospheric Environment*, 42(33), 7775–7785. <https://doi.org/10.1016/j.atmosenv.2008.04.056>
- Calderón-Garcidueñas, L., González-Maciél, A., Mukherjee, P., Reynoso-Robles, R., Pérez-Guillé, B., Gayosso-Chávez, C., et al. (2019). Combustion- and friction-derived magnetic air pollution nanoparticles in human hearts. *Environmental Research*, 176, 108567. <https://doi.org/10.1016/j.envres.2019.108567>
- Calderón-Garcidueñas, L., González-Maciél, A., Reynoso-Robles, R., Hammond, J., Kulesza, R., Lachmann, I., et al. (2020). Quadruple abnormal protein aggregates in brainstem pathology and exogenous metal-rich magnetic nanoparticles (and engineered Ti-rich nanorods). The substantia nigrae is a very early target in young urbanites and the gastrointestinal tract a key brainstem portal. *Environmental Research*, 191, 110139. <https://doi.org/10.1016/j.envres.2020.110139>
- Calderón-Garcidueñas, L., Reynoso-Robles, R., Vargas-Martínez, J., Gómez-Maqueo-Chew, A., Pérez-Guillé, B., Mukherjee, P., et al. (2016). Prefrontal white matter pathology in air pollution exposed Mexico City young urbanites and their potential impact on neurovascular unit dysfunction and the development of Alzheimer's disease. *Environmental Research*, 146, 404–417. <https://doi.org/10.1016/j.envres.2015.12.031>
- Chen, H., Grassian, V., Saraf, L., & Laskin, A. (2013). Chemical imaging analysis of environmental particles using the focused ion beam/scanning electron microscopy technique: Microanalysis insights into atmospheric chemistry of fly ash. *The Analyst*, 138(2), 451–460. <https://doi.org/10.1039/c2an36318f>
- Chen, H., Kwong, J., Copes, R., Tu, K., Villeneuve, P., van Donkelaar, A., et al. (2017). Living near major roads and the incidence of dementia, Parkinson's disease, and multiple sclerosis: A population-based cohort study. *The Lancet*, 389(10070), 718–726. [https://doi.org/10.1016/s0140-6736\(16\)32399-6](https://doi.org/10.1016/s0140-6736(16)32399-6)
- Claquin, T., Schulz, M., & Balkanski, Y. (1999). Modeling the mineralogy of atmospheric dust sources. *Journal of Geophysical Research*, 104(D18), 22243–22256. <https://doi.org/10.1029/1999jd900416>
- Cornell, R., & Schwertmann, U. (2006). *The iron oxides*. Wiley-VCH. <https://onlinelibrary.wiley.com/doi/book/10.1002/3527602097>
- Dankers, P. H. (1978). *Magnetic properties of dispersed natural iron oxides of known grain size* (PhD thesis). University of Utrecht. <https://agris.fao.org/agris-search/search.do?recordID=US201300586721>
- Day, R., Fuller, M., & Schmidt, V. (1977). Hysteresis properties of titanomagnetites: Grain-size and compositional dependence. *Physics of the Earth and Planetary Interiors*, 13(4), 260–267. [https://doi.org/10.1016/0031-9201\(77\)90108-x](https://doi.org/10.1016/0031-9201(77)90108-x)
- Dekkers, M., Mattéi, J., Fillion, G., & Rochette, P. (1989). Grain-size dependence of the magnetic behavior of pyrrhotite during its low-temperature transition at 34 K. *Geophysical Research Letters*, 16(8), 855–858. <https://doi.org/10.1029/g1016i008p00855>
- Devlin, R., Smith, C., Schmitt, M., Rappold, A., Hinderliter, A., Graff, D., & Carraway, M. (2014). Controlled exposure of humans with metabolic syndrome to concentrated ultrafine ambient particulate matter causes cardiovascular effects. *Toxicological Sciences*, 140(1), 61–72. <https://doi.org/10.1093/toxsci/ufu063>
- Dreher, K. L., Jaskot, R. H., Lehmann, J. R., Richards, J. H., Ghio, J. K. M. A. J., & Costa, D. L. (1997). Soluble transition metals mediate residual oil fly ash induced acute lung injury. *Journal of Toxicology and Environmental Health*, 50(3), 285–305. <https://doi.org/10.1080/009841097160492>
- Dunlop, D. (2002). Theory and application of the Day plot (M_s/M_r versus H_c/H_c2). Application to data for rocks, sediments, and soils. *Journal of Geophysical Research*, 107(B3). <https://doi.org/10.1029/2001jb000487>
- Dusseldorp, A., Kruize, H., Brunekreef, B., Hofschreuder, P., de Meer, G., & van Oudvorst, A. (1995). Associations of PM10 and airborne iron with respiratory health of adults living near a steel factory. *American Journal of Respiratory and Critical Care Medicine*, 152(6), 1932–1939. <https://doi.org/10.1164/ajrccm.152.6.8520758>
- Egli, R. (2013). VARIFORC: An optimized protocol for calculating non-regular first-order reversal curve (FORC) diagrams. *Global and Planetary Change*, 110, 302–320. <https://doi.org/10.1016/j.gloplacha.2013.08.003>
- Egli, R., Chen, A., Winklhofer, M., Kodama, K., & Horng, C. (2010). Detection of noninteracting single domain particles using first-order reversal curve diagrams. *Geochemistry, Geophysics, Geosystems*, 11(1). <https://doi.org/10.1029/2009gc002916>
- Einsle, J., Eggeman, A., Martineau, B., Saghi, Z., Collins, S., Blukis, R., et al. (2018). Nanomagnetic properties of the meteorite cloudy zone. *Proceedings of the National Academy of Sciences*, 115(49), E11436–E11445. <https://doi.org/10.1073/pnas.1809378115>
- Einsle, J. F., Harrison, R. J., Kasama, T., Conbhú, P. Ó., Fabian, K., Williams, W., et al. (2016). Multi-scale three-dimensional characterization of iron particles in dusty olivine: Implications for paleomagnetism of chondritic meteorites. *American Mineralogist*, 101(9). <https://doi.org/10.2138/am-2016-5738CCBY>
- Franceschi, V. (2001). Calcium oxalate in plants. *Trends in Plant Science*, 6(7), 331. [https://doi.org/10.1016/s1360-1385\(01\)02014-3](https://doi.org/10.1016/s1360-1385(01)02014-3)
- Gaffney, J., & Marley, N. (2009). The impacts of combustion emissions on air quality and climate – From coal to biofuels and beyond. *Atmospheric Environment*, 43(1), 23–36. <https://doi.org/10.1016/j.atmosenv.2008.09.016>
- Glasauer, S. M., Beveridge, T. J., Burford, E. P., Harper, F. A., & Gadd, G. M. (2013). *Metals and metalloids, transformation by microorganisms. Reference Module in Earth Systems and Environmental Sciences*. Elsevier. <https://doi.org/10.1016/b978-0-12-409548-9.05217-9>
- Gonet, T., & Maher, B. (2019). Airborne, vehicle-derived Fe-bearing nanoparticles in the urban environment: A review. *Environmental Science & Technology*, 53(17), 9970–9991. <https://doi.org/10.1021/acs.est.9b01505>
- Gonet, T., Maher, B., & Kukutschová, J. (2021). Source apportionment of magnetite particles in roadside airborne particulate matter. *Science of the Total Environment*, 752, 141828. <https://doi.org/10.1016/j.scitotenv.2020.141828>
- Gonet, T., Maher, B., Nyirő-Kósa, I., Pósfai, M., Vaculík, M., & Kukutschová, J. (2021). Size-resolved, quantitative evaluation of the magnetic mineralogy of airborne brake-wear particulate emissions. *Environmental Pollution*, 288, 117808. <https://doi.org/10.1016/j.envpol.2021.117808>
- Harrison, R. J., & Feinberg, J. M. (2008). FORCinel: An improved algorithm for calculating first-order reversal curve distributions using locally weighted regression smoothing. *Geochemistry, Geophysics, Geosystems*, 9(5). <https://doi.org/10.1029/2008gc001987>
- Harrison, R. J., & Lascu, I. (2014). FORCulator: A micromagnetic tool for simulating first-order reversal curve diagrams. *Geochemistry, Geophysics, Geosystems*, 15(12), 4671–4691. <https://doi.org/10.1002/2014GC005582>
- Harrison, R. J., Muraszko, J., Heslop, D., Lascu, I., Muxworthy, A. R., & Roberts, A. P. (2018). An improved algorithm for unmixing first-order reversal curve diagrams using principal component analysis. *Geochemistry, Geophysics, Geosystems*, 19(5), 1595–1610. <https://doi.org/10.1029/2018gc007511>
- Harrison, R. M., Jones, A. M., Gietl, J., Yin, J., & Green, D. C. (2012). Estimation of the contributions of brake dust, tire wear, and resuspension to nonexhaust traffic particles derived from atmospheric measurements. *Environmental Science & Technology*, 46(12), 6523–6529. <https://doi.org/10.1021/es300894r>

- Hofman, J., Castanheiro, A., Nuyts, G., Joosen, S., Spassov, S., Blust, R., et al. (2020). Impact of urban street canyon architecture on local atmospheric pollutant levels and magneto-chemical PM10 composition: An experimental study in Antwerp, Belgium. *Science of the Total Environment*, 712, 135534. <https://doi.org/10.1016/j.scitotenv.2019.135534>
- Hofman, J., Wuyts, K., Van Wittenberghe, S., Brackx, M., & Samson, R. (2014). On the link between biomagnetic monitoring and leaf-deposited dust load of urban trees: Relationships and spatial variability of different particle size fractions. *Environmental Pollution*, 189, 63–72. <https://doi.org/10.1016/j.envpol.2014.02.020>
- Hofman, J., Wuyts, K., Van Wittenberghe, S., & Samson, R. (2014). On the temporal variation of leaf magnetic parameters: Seasonal accumulation of leaf-deposited and leaf-encapsulated particles of a roadside tree crown. *Science of the Total Environment*, 493, 766–772. <https://doi.org/10.1016/j.scitotenv.2014.06.074>
- Jeanjean, A., Buccolieri, R., Eddy, J., Monks, P., & Leigh, R. (2017). Air quality affected by trees in real street canyons: The case of Marylebone neighbourhood in central London. *Urban Forestry & Urban Greening*, 22, 41–53. <https://doi.org/10.1016/j.ufug.2017.01.009>
- Kardel, F., Wuyts, K., Maher, B., Hansard, R., & Samson, R. (2011). Leaf saturation isothermal remanent magnetization (SIRM) as a proxy for particulate matter monitoring: Inter-species differences and in-season variation. *Atmospheric Environment*, 45(29), 5164–5171. <https://doi.org/10.1016/j.atmosenv.2011.06.025>
- Kelly, F., & Fussell, J. (2012). Size, source and chemical composition as determinants of toxicity attributable to ambient particulate matter. *Atmospheric Environment*, 60, 504–526. <https://doi.org/10.1016/j.atmosenv.2012.06.039>
- Lagroix, F., & Guyodo, Y. (2017). A new tool for separating the magnetic mineralogy of complex mineral assemblages from low temperature magnetic behavior. *Frontiers in Earth Science*, 5. <https://doi.org/10.3389/feart.2017.00061>
- Lanci, L., & Kent, D. V. (2018). Forward modeling of thermally activated single-domain magnetic particles applied to first-order reversal curves. *Journal of Geophysical Research: Solid Earth*, 123(5), 3287–3300. <https://doi.org/10.1002/2018JB015463>
- Lappe, S.-C. L. L., Church, N. S., Kasama, T., da Silva Fanta, A. B., Bromiley, G., Dunin-Borkowski, R. E., et al. (2011). Mineral magnetism of dusty olivine: A credible recorder of pre-accretionary remanence. *Geochemistry, Geophysics, Geosystems*, 12(12), Q12Z35. <https://doi.org/10.1029/2011GC003811>
- Lappe, S.-C. L. L., Feinberg, J. M., Muxworthy, A., & Harrison, R. J. (2013). Comparison and calibration of nonheating paleointensity methods: A case study using dusty olivine. *Geochemistry, Geophysics, Geosystems*, 14(7), 2143–2158. <https://doi.org/10.1002/ggge.20141>
- Lascu, I., Banerjee, S., & Berquó, T. (2010). Quantifying the concentration of ferrimagnetic particles in sediments using rock magnetic methods. *Geochemistry, Geophysics, Geosystems*, 11(8). <https://doi.org/10.1029/2010gc003182>
- Lascu, I., Einsle, J., Ball, M., & Harrison, R. (2018). The vortex state in geologic materials: A micromagnetic perspective. *Journal of Geophysical Research: Solid Earth*, 123(9), 7285–7304. <https://doi.org/10.1029/2018jb015909>
- Lascu, I., Harrison, R., Li, Y., Muraszko, J., Channell, J., Piotrowski, A., & Hodell, D. (2015). Magnetic unmixing of first-order reversal curve diagrams using principal component analysis. *Geochemistry, Geophysics, Geosystems*, 16(9), 2900–2915. <https://doi.org/10.1002/2015gc005909>
- Lehndorff, E., & Schwark, L. (2004). Biomonitoring of air quality in the Cologne Conurbation using pine needles as a passive sampler—Part II: Polycyclic aromatic hydrocarbons (PAH). *Atmospheric Environment*, 38(23), 3793–3808. <https://doi.org/10.1016/j.atmosenv.2004.03.065>
- Leitte, A., Schlink, U., Herbarth, O., Wiedensohler, A., Pan, X., Hu, M., et al. (2012). Associations between size-segregated particle number concentrations and respiratory mortality in Beijing, China. *International Journal of Environmental Health Research*, 22(2), 119–133. <https://doi.org/10.1080/09603123.2011.605878>
- Li, W., & Shao, L. (2009). Transmission electron microscopy study of aerosol particles from the brown hazes in northern China. *Journal of Geophysical Research*, 114(D9). <https://doi.org/10.1029/2008jd011285>
- Li, W., Shao, L., & Buseck, P. (2010). Haze types in Beijing and the influence of agricultural biomass burning. *Atmospheric Chemistry and Physics*, 10(17), 8119–8130. <https://doi.org/10.5194/acp-10-8119-2010>
- Lodhi, A., Ghauri, B., Khan, M., Rahman, S., & Shafique, S. (2009). Particulate matter (PM_{2.5}) concentration and source apportionment in Lahore. *Journal of the Brazilian Chemical Society*, 20(10), 1811–1820. <https://doi.org/10.1590/s0103-50532009001000007>
- Maher, B. (1988). Magnetic properties of some synthetic sub-micron magnetites. *Geophysical Journal International*, 94(1), 83–96. <https://doi.org/10.1111/j.1365-246x.1988.tb03429.x>
- Maher, B. (2019). Airborne magnetite- and iron-rich pollution nanoparticles: Potential neurotoxicants and environmental risk factors for neurodegenerative disease, including Alzheimer's disease. *Journal of Alzheimer's Disease*, 71(2), 361–375. <https://doi.org/10.3233/jad-190204>
- Maher, B., Ahmed, I., Davison, B., Karloukovski, V., & Clarke, R. (2013). Impact of roadside tree lines on indoor concentrations of traffic-derived particulate matter. *Environmental Science & Technology*, 47(23), 13737–13744. <https://doi.org/10.1021/es404363m>
- Maher, B., Ahmed, I., Karloukovski, V., MacLaren, D., Foulds, P., Allsop, D., et al. (2016). Magnetite pollution nanoparticles in the human brain. *Proceedings of the National Academy of Sciences*, 113(39), 10797–10801. <https://doi.org/10.1073/pnas.1605941113>
- Maher, B., González-Maciel, A., Reynoso-Robles, R., Torres-Jardón, R., & Calderón-Garcidueñas, L. (2020). Iron-rich air pollution nanoparticles: An unrecognized environmental risk factor for myocardial mitochondrial dysfunction and cardiac oxidative stress. *Environmental Research*, 188, 109816. <https://doi.org/10.1016/j.envres.2020.109816>
- Maher, B., Moore, C., & Matzka, J. (2008). Spatial variation in vehicle-derived metal pollution identified by magnetic and elemental analysis of roadside tree leaves. *Atmospheric Environment*, 42(2), 364–373. <https://doi.org/10.1016/j.atmosenv.2007.09.013>
- Maher, B., & Taylor, R. (1988). Formation of ultrafine-grained magnetite in soils. *Nature*, 336(6197), 368–370. <https://doi.org/10.1038/336368a0>
- Maher, B., & Thompson, R. (1999). *Quaternary climates, environments and magnetism*. Cambridge University Press.
- Matzka, J., & Maher, B. (1999). Magnetic biomonitoring of roadside tree leaves: Identification of spatial and temporal variations in vehicle-derived particulates. *Atmospheric Environment*, 33(28), 4565–4569. [https://doi.org/10.1016/s1352-2310\(99\)00229-0](https://doi.org/10.1016/s1352-2310(99)00229-0)
- Miller, M., Raftis, J., Langrish, J., McLean, S., Samutrtai, P., Connell, S., et al. (2017). Correction to “Inhaled nanoparticles accumulate at sites of vascular disease”. *ACS Nano*, 11(10), 10623–10624. <https://doi.org/10.1021/acsnano.7b06327>
- Mitchell, R., & Maher, B. (2009). Evaluation and application of biomagnetic monitoring of traffic-derived particulate pollution. *Atmospheric Environment*, 43(13), 2095–2103. <https://doi.org/10.1016/j.atmosenv.2009.01.042>
- Muhammad, S., Wuyts, K., & Samson, R. (2019). Atmospheric net particle accumulation on 96 plant species with contrasting morphological and anatomical leaf characteristics in a common garden experiment. *Atmospheric Environment*, 202, 328–344. <https://doi.org/10.1016/j.atmosenv.2019.01.015>
- Muxworthy, A. R., Matzka, J., Davila, A., & Petersen, N. (2003). Magnetic signature of daily sampled urban atmospheric particles. *Atmospheric Environment*, 37(29), 4163–4169. [https://doi.org/10.1016/s1352-2310\(03\)00500-4](https://doi.org/10.1016/s1352-2310(03)00500-4)
- Muxworthy, A. R., Schmidbauer, E., & Petersen, N. (2002). Magnetic properties and Mössbauer spectra of urban atmospheric particulate matter: A case study from Munich, Germany. *Geophysical Journal International*, 150(2), 558–570. <https://doi.org/10.1046/j.1365-246x.2002.01725.x>
- Muxworthy, A. R., & Williams, W. (2015). Critical single-domain grain sizes in elongated iron particles: Implications for meteoritic and lunar magnetism. *Geophysical Journal International*, 202(1), 578–583. <https://doi.org/10.1093/gji/ggv180>

- Nagy, L., Williams, W., Tauxe, L., Muxworthy, A. R., & Ferreira, I. (2019). Thermomagnetic recording fidelity of nanometer-sized iron and implications for planetary magnetism. *Proceedings of the National Academy of Sciences*, *116*(6), 1984–1991. <https://doi.org/10.1073/pnas.1810797116>
- Nel, A., Xia, T., Mädler, L., & Li, N. (2006). Toxic potential of materials at the nanolevel. *Science*, *311*(5761), 622–627. <https://doi.org/10.1126/science.1114397>
- Newell, A. J. (2005). A high-precision model of first-order reversal curve (FORC) functions for single-domain ferromagnets with uniaxial anisotropy. *Geochemistry, Geophysics, Geosystems*, *6*(5), Q05010. <https://doi.org/10.1029/2004GC000877>
- Niemi, J., Saarikoski, S., Tervahattu, H., Mäkelä, T., Hillamo, R., Vehkamäki, H., et al. (2006). Changes in background aerosol composition in Finland during polluted and clean periods studied by TEM/EDX individual particle analysis. *Atmospheric Chemistry and Physics*, *6*(12), 5049–5066. <https://doi.org/10.5194/acp-6-5049-2006>
- Ohlwein, S., Kappeler, R., Kutlar Joss, M., Künzli, N., & Hoffmann, B. (2019). Health effects of ultrafine particles: A systematic literature review update of epidemiological evidence. *International Journal of Public Health*, *64*(4), 547–559. <https://doi.org/10.1007/s00038-019-01202-7>
- Özdemir, Ö., & Banerjee, S. (1982). A preliminary magnetic study of soil samples from west-central Minnesota. *Earth and Planetary Science Letters*, *59*(2), 393–403. [https://doi.org/10.1016/0012-821x\(82\)90141-8](https://doi.org/10.1016/0012-821x(82)90141-8)
- Özdemir, Ö., & Dunlop, D. (2010). Hallmarks of maghemitization in low-temperature remanence cycling of partially oxidized magnetite nanoparticles. *Journal of Geophysical Research*, *115*(B2). <https://doi.org/10.1029/2009jb006756>
- Özdemir, Ö., Dunlop, D., & Moskowitz, B. (1993). The effect of oxidation on the Verwey transition in magnetite. *Geophysical Research Letters*, *20*(16), 1671–1674. <https://doi.org/10.1029/93gl01483>
- Penttinen, P., Timonen, K., Tiittanen, P., Mirme, A., Ruuskanen, J., & Pekkanen, J. (2001). Ultrafine particles in urban air and respiratory health among adult asthmatics. *European Respiratory Journal*, *17*(3), 428–435. <https://doi.org/10.1183/09031936.01.17304280>
- Pike, C., Roberts, A., & Verosub, K. (1999). Characterizing interactions in fine magnetic particle systems using first order reversal curves. *Journal of Applied Physics*, *85*(9), 6660–6667. <https://doi.org/10.1063/1.370176>
- Rea-Downing, G., Quirk, B., Wagner, C., & Lippert, P. (2020). Evergreen needle magnetization as a proxy for particulate matter pollution in urban environments. *Geohealth*, *4*(9). <https://doi.org/10.1029/2020gh000286>
- Roberts, A., Pike, C., & Verosub, K. (2000). First-order reversal curve diagrams: A new tool for characterizing the magnetic properties of natural samples. *Journal of Geophysical Research*, *105*(B12), 28461–28475. <https://doi.org/10.1029/2000jb900326>
- Roberts, A. P., Tauxe, L., Heslop, D., Zhao, X., & Jiang, Z. (2018). A critical appraisal of the “Day” diagram. *Journal of Geophysical Research: Solid Earth*. <https://doi.org/10.1002/2017JB015247>
- Rückerl, R., Schneider, A., Breitner, S., Cyrys, J., & Peters, A. (2011). Health effects of particulate air pollution: A review of epidemiological evidence. *Inhalation Toxicology*, *23*(10), 555–592. <https://doi.org/10.3109/08958378.2011.593587>
- Saarikoski, S., Timonen, H., Saarnio, K., Aurela, M., Järvi, L., Keronen, P., et al. (2008). Sources of organic carbon in fine particulate matter in northern European urban air. *Atmospheric Chemistry and Physics*, *8*(20), 6281–6295. <https://doi.org/10.5194/acp-8-6281-2008>
- Sagnotti, L., Macrì, P., Egli, R., & Mondino, M. (2006). Magnetic properties of atmospheric particulate matter from automatic air sampler stations in Latium (Italy): Toward a definition of magnetic fingerprints for natural and anthropogenic PM10 sources. *Journal of Geophysical Research: Solid Earth*, *111*(B12). <https://doi.org/10.1029/2006jb004508>
- Sagnotti, L., Taddeucci, J., Winkler, A., & Cavallo, A. (2009). Compositional, morphological, and hysteresis characterization of magnetic airborne particulate matter in Rome, Italy. *Geochemistry, Geophysics, Geosystems*, *10*(8). <https://doi.org/10.1029/2009gc002563>
- Schraufnagel, D. E. (2020). The health effects of ultrafine particles. *Experimental and Molecular Medicine*, *52*(3), 311–317. <https://doi.org/10.1038/s12276-020-0403-3>
- Schwarze, P., Øvrevik, J., Låg, M., Refsnes, M., Nafstad, P., Hetland, R., & Dybing, E. (2006). Particulate matter properties and health effects: Consistency of epidemiological and toxicological studies. *Human & Experimental Toxicology*, *25*(10), 559–579. <https://doi.org/10.1177/096032706072520>
- Seaton, A., Godden, D., MacNee, W., & Donaldson, K. (1995). Particulate air pollution and acute health effects. *The Lancet*, *345*(8943), 176–178. [https://doi.org/10.1016/s0140-6736\(95\)90173-6](https://doi.org/10.1016/s0140-6736(95)90173-6)
- Selley, L., Schuster, L., Marbach, H., Forsthuber, T., Forbes, B., Gant, T., et al. (2020). Brake dust exposure exacerbates inflammation and transiently compromises phagocytosis in macrophages. *Metallomics*, *12*(3), 371–386. <https://doi.org/10.1039/c9mt00253g>
- Shah, M., Shaheen, N., & Nazir, R. (2012). Assessment of the trace elements level in urban atmospheric particulate matter and source apportionment in Islamabad, Pakistan. *Atmospheric Pollution Research*, *3*(1), 39–45. <https://doi.org/10.5094/apr.2012.003>
- Shaheen, N., Shah, M., Khaliq, A., & Jaffar, M. (2005). Metal levels in airborne particulate matter in urban Islamabad, Pakistan. *Bulletin of Environmental Contamination and Toxicology*, *75*(4), 739–746. <https://doi.org/10.1007/s00128-005-0813-x>
- Silva, P., Liu, D., Noble, C., & Prather, K. (1999). Size and chemical characterization of individual particles resulting from biomass burning of local southern California species. *Environmental Science & Technology*, *33*(18), 3068–3076. <https://doi.org/10.1021/es980544p>
- Smirnov, A. (2009). Grain size dependence of low-temperature remanent magnetization in natural and synthetic magnetite: Experimental study. *Earth, Planets and Space*, *61*(1), 119–124. <https://doi.org/10.1186/bf03352891>
- Smith, M., Harris, P., Sayre, L., & Perry, G. (1997). Iron accumulation in Alzheimer disease is a source of redox-generated free radicals. *Proceedings of the National Academy of Sciences*, *94*(18), 9866–9868. <https://doi.org/10.1073/pnas.94.18.9866>
- Spassov, S., Egli, R., Heller, F., Nourgaliev, D., & Hannam, J. (2004). Magnetic quantification of urban pollution sources in atmospheric particulate matter. *Geophysical Journal International*, *159*(2), 555–564. <https://doi.org/10.1111/j.1365-246x.2004.02438.x>
- Stone, E., Schauer, J., Quraishi, T., & Mahmood, A. (2010). Chemical characterization and source apportionment of fine and coarse particulate matter in Lahore, Pakistan. *Atmospheric Environment*, *44*(8), 1062–1070. <https://doi.org/10.1016/j.atmosenv.2009.12.015>
- Tong, Z., Baldauf, R., Isakov, V., Deshmukh, P., & Max Zhang, K. (2016). Roadside vegetation barrier designs to mitigate near-road air pollution impacts. *Science of the Total Environment*, *541*, 920–927. <https://doi.org/10.1016/j.scitotenv.2015.09.067>
- Verwey, E. J. W. (1939). Electronic conduction of magnetite (Fe₃O₄) and its transition point at low temperatures. *Nature*, *144*, 327. <https://doi.org/10.1038/144327b0>
- Wang, H., Maher, B., Ahmed, I., & Davison, B. (2019). Efficient removal of ultrafine particles from diesel exhaust by selected tree species: Implications for roadside planting for improving the quality of urban air. *Environmental Science & Technology*, *53*(12), 6906–6916. <https://doi.org/10.1021/acs.est.8b06629>
- Winkler, A., Amoroso, A., Di Giosa, A., & Marchegiani, G. (2021). The effect of Covid-19 lockdown on airborne particulate matter in Rome, Italy: A magnetic point of view. *Environmental Pollution*, *291*, 118191. <https://doi.org/10.1016/j.envpol.2021.118191>
- Winkler, A., Contardo, T., Vannini, A., Sorbo, S., Basile, A., & Loppi, S. (2020). Magnetic emissions from brake wear are the major source of airborne particulate matter bioaccumulated by lichens exposed in Milan (Italy). *Applied Sciences*, *10*(6), 2073. <https://doi.org/10.3390/app10062073>

- Yuan, Y., Wu, Y., Ge, X., Nie, D., Wang, M., Zhou, H., & Chen, M. (2019). In vitro toxicity evaluation of heavy metals in urban air particulate matter on human lung epithelial cells. *Science of the Total Environment*, 678, 301–308. <https://doi.org/10.1016/j.scitotenv.2019.04.431>
- Zhang, X., Chen, X., & Zhang, X. (2018). The impact of exposure to air pollution on cognitive performance. *Proceedings of the National Academy of Sciences*, 115(37), 9193–9197. <https://doi.org/10.1073/pnas.1809474115>

References From the Supporting Information

- Buseck, P., Adachi, K., Gelencsér, A., Tompa, É., & Pósfai, M. (2014). Ns-Soot: A material-based term for strongly light-absorbing carbonaceous particles. *Aerosol Science & Technology*, 48(7), 777–788. <https://doi.org/10.1080/02786826.2014.919374>
- Coelho, A. (2018). TOPAS and TOPAS-Academic: An optimization program integrating computer algebra and crystallographic objects written in C++. *Journal of Applied Crystallography*, 51(1), 210–218. <https://doi.org/10.1107/s1600576718000183>
- Dollase, W. A. (1986). Correction of intensities for preferred orientation in powder diffractometry: Application of the March model. *Journal of Applied Crystallography*, 19(4), 267–272. <https://doi.org/10.1107/s0021889886089458>
- Hellenbrandt, M. (2004). The inorganic crystal structure database (ICSD)—Present and future. *Crystallography Reviews*, 10(1), 17–22. <https://doi.org/10.1080/08893110410001664882>
- Madsen, I. C., & Scarlett, N. V. Y. (2008). Quantitative phase analysis. In R. E. Dinnebier (Ed.), *Powder diffraction: Theory and practice*. Royal Society of Chemistry.
- Shi, Z., Shao, L., Jones, T., Whittaker, A., Lu, S., Bérubé, K., et al. (2003). Characterization of airborne individual particles collected in an urban area, a satellite city and a clean air area in Beijing, 2001. *Atmospheric Environment*, 37(29), 4097–4108. [https://doi.org/10.1016/s1352-2310\(03\)00531-4](https://doi.org/10.1016/s1352-2310(03)00531-4)